Photon and dilepton production at the Facility for Antiproton and Ion Research and beam-energy scan at the Relativistic Heavy-Ion Collider using coarse-grained microscopic transport simulations

Stephan Endres,* Hendrik van Hees, and Marcus Bleicher
Frankfurt Institute for Advanced Studies, Ruth-Moufang-Strasse 1, D-60438 Frankfurt, Germany
and Institut für Theoretische Physik, Universität Frankfurt, Max-von-Laue-Strasse 1, D-60438 Frankfurt, Germany
(Received 21 December 2015; revised manuscript received 7 April 2016; published 2 May 2016; corrected 13 May 2016)

We present calculations of dilepton and photon spectra for the energy range $E_{\mathrm{lab}} = 2A$ to $35A$ GeV which will be available for the Compressed Baryonic Matter (CBM) experiment at the future Facility for Antiproton and Ion Research (FAIR). The same energy regime will also be covered by phase II of the beam-energy scan at the Relativistic Heavy-Ion Collider (RHIC-BES). Coarse-grained dynamics from microscopic transport calculations of the Ultrarelativistic Quantum Molecular Dynamics (UrQMD) model is used to determine temperature and chemical potentials, which allows for the use of dilepton and photon-emission rates from equilibrium quantum-field-theory calculations. The results indicate that nonequilibrium effects, the presence of baryonic matter, and the creation of a deconfined phase might show up in specific manners in the measurable dilepton invariant-mass spectra and in the photon transverse-momentum spectra. However, as the many influences are difficult to disentangle, we argue that the challenge for future measurements of electromagnetic probes will be to provide a high precision with uncertainties much lower than in previous experiments. Furthermore, a systematic study of the whole energy range covered by CBM at FAIR and RHIC-BES is necessary to discriminate between different effects, which influence the spectra, and to identify possible signatures of a phase transition.

DOI: 10.1103/PhysRevC.93.054901

I. INTRODUCTION

A major goal of the study of heavy-ion collisions at relativistic and ultrarelativistic collision energies is to explore the properties of strongly interacting matter at finite temperatures and densities [1,2]. When two colliding nuclei hit each other, the nuclear matter is compressed, and a large amount of energy is deposited in a small spatial volume. This results in the creation of a fireball of hot and dense matter [3,4]. The fireball lives for a time span of the order of several fm/c until the collective expansion of the matter has driven the strongly interacting system to a final state of freely streaming particles.

Today, almost the entire phase diagram governed by quantum chromodynamics (QCD) is accessible for experimental exploration at various accelerator facilities. The temperature T and baryochemical potential μ_{B} inside the fireball are mainly determined by the energy which is deposited in the nuclear collision; more precisely, the collision energy determines the trajectory of the system in the T-μ_{B} plane of the QCD phase diagram. At the highest currently available energies at the BNL Relativistic Heavy-Ion Collider (RHIC) and at the CERN Large Hadron Collider (LHC), the reaction is dominated by high temperatures, significantly above the critical temperature T_c, for which the creation of a deconfined state of quarks and gluons is assumed. At the same time, the baryochemical potential is low or close to zero for the largest part of the fireball evolution. This situation is similar to the conditions which prevailed in the universe a short time after the big bang. On the other side, one finds a complementary situation if considering heavy-ion collisions at laboratory-frame energies of the order of $1A$ GeV. Here only moderate temperatures are obtained, insufficient to create a quark-gluon plasma. However, the very high net baryon densities or baryochemical potentials reached in this case might provide valuable information about those effects which are not mainly driven by temperature but by the presence of compressed baryonic matter. This situation resembles the environments in (super)nova explosions and neutron stars.

To learn about the different regions of the phase diagram, one needs observables which do not only reflect the diluted final state after the freeze-out of the system but rather convey information about the entire fireball evolution. For this purpose, electromagnetic probes, i.e., photons and dileptons, have long been suggested as ideal probes [5,6]: Once produced, photons and dileptons only participate in electromagnetic and weak interactions for which the mean-free paths are much longer than the size and the lifetime of the fireball. Consequently, they can leave the zone of hot and dense matter undisturbed. Since electromagnetic probes are emitted in a large variety of processes over the whole lifetime of the fireball, the measured spectra reflect the time-integrated evolution of the thermodynamic properties of the system. While this allows us to obtain convoluted information about the properties of matter, it also poses a serious challenge for the theoretical description. On the one hand, one needs to identify the relevant microscopic processes that contribute to dilepton and photon emission and to determine the corresponding production rates. On the other hand it is important to give a realistic description of the complete reaction dynamics.

The intense experimental study of photon and dilepton production in the high-energy regime [at CERN Super Proton Synchrotron (SPS) [7–9], RHIC [10–13], and LHC [14] energies], but also for very low collision energies as measured

*endres@th.physik.uni-frankfurt.de

at SIS 18 and BEVALAC [15–18] in comparison to theoretical model calculations has significantly enhanced our knowledge of the reaction dynamics and the properties of matter in the hot and dense medium created in a heavy-ion reaction. The importance of partonic emission for the correct theoretical description of the high-mass region of dilepton invariant-mass spectra and the high-p_t photon spectra has been pointed out [19–21] and the various different hadronic contributions (especially for the photon production channels) could be identified [22–24]. Nevertheless, the most important finding was the large influence of the baryonic matter on the vector mesons' spectral shape. Especially in the case of the ρ meson this causes a strong broadening of the spectral function with small mass shifts [25–28]. This effect has been observed as an enhancement in the low-mass region of the dilepton invariant-mass spectra and also shows up as a stronger low-momentum thermal photon yield. Note that the ρ broadening is most dominant at low collision energies, where one obtains the largest baryochemical potentials, but even at RHIC energies baryonic effects are by far not negligible.

However, there still remains an up-to-now unexplored energy window between the $E_{\mathrm{lab}} = 1A$–$2A$ GeV dilepton measurements by the DLS and HADES Collaborations and the CERES results for $E_{\mathrm{lab}} = 40A$ GeV. The future compressed baryonic matter (CBM) experiment at the Facility for Antiproton and Ion Research (FAIR) with the SIS 100 and SIS 300 accelerator provides the unique possibility to study heavy-ion collisions with beam energies from $2A$ up to $35A$ GeV and will therefore enable us to get an insight into exactly that regime of the phase diagram of highest baryon densities where no dilepton or photon measurements have been performed until now [29,30]. In addition, also phase II of the beam-energy scan (BES) program at RHIC will allow for measurements in fixed-target mode at laboratory-frame energies of $7.7A$, $9.1A$, $11.5A$, $14.5A$, and $19.6A$ GeV, i.e., in the same collision-energy range as FAIR [31]. Further complementary investigations are also planned for the Nuclotron-Based Ion Collider Facility (NICA) in Dubna [32].

From a theoretical point of view, the handling of this energy range is quite challenging, because the transition from a purely hadronic fireball at low collision energies to the creation of a partonic phase is expected here. Furthermore, at the high baryochemical potentials which still dominate the fireball at these energies, a first-order phase transition from a hadron gas to the QGP is assumed, in contrast with the situation at RHIC or the LHC where a crossover is predicted by lattice QCD calculations [33].

Although transport models were applied successfully to describe electromagnetic observables in heavy-ion collisions [34–36], they generally have some shortcomings when describing very hot and dense systems. In detail, problems include the following aspects: First, while the Boltzmann approach works quite well for quasiparticles of infinite lifetime, for broad resonances, such as the ρ meson, a correct description is challenging. Furthermore, in dense matter the intervals between scatterings become extremely short and will consequently modify the spectral characteristics of the single particles (collisional broadening). To describe the off-shell dynamics correctly a transport description with dynamical spectral functions following the description of Kadanoff and Baym [37] is required. However, a practical implementation of this is currently not possible. Second, in a dense medium not only binary scatterings occur but multiparticle interactions also play a role, which is beyond the capabilities of the common transport models. And finally, the microscopic models usually concentrate on either the transport of hadrons or partons. However, modelling a transition from an initially up-heating hadron gas to a deconfined phase and the later particlization when the system cools down is extremely difficult to realize within a transport approach.

There have been several investigations over the last years of these aspects (see, e.g., Refs. [38–44]), but a full treatment of all these issues is still beyond the scope of present investigations.

On the other side, the short mean-free paths of particles in a medium might suggest treating the reactions from a macroscopic point of view. However, approaches such as simple fireball expansion models [45] or hydrodynamics [46], which have been successfully applied for SPS, RHIC, and LHC energies, also have their shortcomings in the FAIR energy regime for three main reasons: First, the separation of the fireball expansion from dynamics of the initial projectile-target dynamics is not applicable; second, the often-applied simplification to assume a $(2 + 1)$-dimensional boost-invariant geometry is not possible; and finally, the timescale necessary for an approximate thermal equilibration of the fireball will be longer due to the slower overall evolution of the reaction and the lower temperatures reached.

To avoid the disadvantages of both pictures, the coarse-graining method was developed based on previous studies [47] and was successfully applied to describe dilepton production at SPS and SIS 18 energies [27,28,48]. The approach represents a combination of the microscopic picture from the underlying transport simulations with the resulting description of the dynamics in terms of the macroscopic quantities temperature and chemical potential. By averaging over many events one can extract the local energy and baryon densities at each space-time point from the transport simulations and use an equation of state to determine the corresponding temperature and baryochemical potential. With this, the calculation method of thermal dilepton and photon emission by application of full in-medium spectral functions is straightforward, employing the rates available from equilibrium quantum field theory.

In the present work, the coarse-graining approach is used to calculate photon and dilepton spectra with focus being the FAIR energy regime, but naturally the results also serve as a theoretical prediction for the fixed-target measurements of the RHIC-BES since the prospected collision energies of both experimental programs overlap. Although the details of the future experimental setups are not yet determined, the results shall provide a general baseline calculation for the interpretation of the measurements to be conducted. Furthermore, it shall be investigated if and how one can obtain valuable information on the properties of matter from the measured spectra and discriminate between several effects that might influence the dilepton and photon results. In detail, we will concentrate on the following three aspects: the modification of the thermal emission pattern by high baryochemical potentials, signals for

a phase transition or the creation of a deconfined phase, and possible nonequilibrium effects on the thermal rates.

This paper is structured as follows: In Sec. II the coarse-graining approach will be presented. Thereafter, in Sec. III we introduce the various microscopic sources for thermal emission of photons and dileptons and, in short, discuss the nonthermal cocktail contributions. In Sec. IV the results for the fireball evolution and the photon and dilepton spectra at FAIR energies are shown. The results are used to systematically analyze in which way it might be possible to discriminate between different scenarios for the fireball evolution in Sec. V. We conclude the present work with a summary and an outlook to subsequent investigations.

II. THE MODEL

While microscopic transport models describe the reaction dynamics of a heavy-ion collision in terms of many different degrees of freedom, the general idea of the coarse-graining approach is that, in principle, only a very reduced amount of the provided information is necessary to account for the thermal production of electromagnetic probes. The microscopic information about all individual particles and their specific properties, such as mass, charge and momentum, are ignored and the whole dynamics is reduced to macroscopic quantities, which are assumed to fully determine the local thermodynamic properties: the energy and particle densities.

The coarse-graining method combines two advantages: On the one hand, the collision dynamics is still based on the microscopic transport evolution and thereby gives a very nuanced picture of the entire collision evolution. On the other hand, the reduction to macroscopic state variables enables an easy application of in-medium spectral functions from equilibrium quantum-field-theory calculations.

In the following the ingredients of the approach are presented in detail.

A. Ultrarelativistic Quantum Molecular Dynamics

The underlying microscopic input for the present calculations stems from the Ultrarelativistic Quantum Molecular Dynamics (UrQMD) approach [49–51]. It is a nonequilibrium microscopic transport model based on the principles of molecular dynamics [52,53]. It constitutes an effective Monte Carlo solution to the relativistic Boltzmann equation and connects the propagation of hadrons on covariant trajectories with a probabilistic description of the hadron-hadron scattering processes. To account for the quantum nature of the particles, each hadron is represented by a Gaussian density distribution, and quantum statistical effects such as Pauli blocking are considered [54].

The model includes all relevant mesonic and baryonic resonances up to a mass of 2.2 GeV$/c^2$. Production of particles occurs via resonant scattering of particles (e.g., $NN \rightarrow N\Delta$ or $\pi\pi \rightarrow \rho$) or the decay of higher resonances, e.g., the process $\Delta \rightarrow \pi N$. The individual interaction and decay processes are described in terms of measured and extrapolated hadronic cross sections and branching ratios. For collision energies above $\sqrt{s_{NN}} = 3$ GeV, the excitation of strings is also possible.

B. Coarse graining of microscopic dynamics

Within the UrQMD model, the particle distribution function $f(\vec{x},\vec{p},t)$ is determined by the space and momentum coordinates of all the different particles in the system at a certain time. However, due to the finite number h of hadronic particles involved and produced in a heavy-ion collision, one needs to take the average over a large ensemble of events to obtain a smooth phase-space distribution of the form

$$f(\vec{x},\vec{p},t) = \left\langle \sum_h \delta^{(3)}(\vec{x} - \vec{x}_h(t))\delta^{(3)}(\vec{p} - \vec{p}_h(t)) \right\rangle. \quad (1)$$

Note that this distribution is Lorentz invariant if all particles are on the mass shell, as provided in our case. Due to the nonequilibrium nature of the model, one will of course have to extract the particle distribution function locally. In the present approach, this is done by the use of a grid of small space-time cells where, for each of these cells, we determine the (net-) baryon four-flow and the energy-momentum tensor according to the relations

$$j^\mu_{\mathrm{B}} = \int d^3p \frac{p^\mu}{p^0} f^{\mathrm{B}}(\vec{x},\vec{p},t), \quad (2)$$

$$T^{\mu\nu} = \int d^3p \frac{p^\mu p^\nu}{p^0} f(\vec{x},\vec{p},t). \quad (3)$$

In practice, the integration is done by summing over the δ functions. Because we use cells of finite size, we have

$$\delta^{(3)}(\vec{x} - \vec{x}_h(t)) = \begin{cases} \frac{1}{\Delta V} & \text{if } \vec{x}_h(t) \in \Delta V \\ 0 & \text{otherwise,} \end{cases} \quad (4)$$

and in the limit of small volumes the density of some observable $\hat{O}$ then becomes

$$\int d^3p\ \hat{O}(\vec{x},\vec{p},t) f(\vec{x},\vec{p},t) = \frac{1}{\Delta V} \left\langle \sum_h^{\vec{x}_h \in \Delta V} \hat{O}(\vec{x},\vec{p},t) \right\rangle. \quad (5)$$

Consequently, Eqs. (2) and (3) take the form

$$\begin{aligned} T^{\mu\nu} &= \frac{1}{\Delta V} \left\langle \sum_{i=1}^{N_h \in \Delta V} \frac{p_i^\mu \cdot p_i^\nu}{p_i^0} \right\rangle, \\ j^\mu_{\mathrm{B}} &= \frac{1}{\Delta V} \left\langle \sum_{i=1}^{N_{\mathrm{B}/\bar{\mathrm{B}}} \in \Delta V} \pm \frac{p_i^\mu}{p_i^0} \right\rangle. \end{aligned} \quad (6)$$

Having obtained the baryon flow, we can boost each cell into the rest frame as defined by Eckart [55], where j^{B}_μ is $(\rho_{\mathrm{B}},\vec{0})$. The according transformation of the energy-momentum tensor provides the rest-frame energy density.

C. Nonequilibrium dynamics

While macroscopic models usually introduce thermal and chemical equilibrium as an ad hoc assumption, microscopic simulations—in the present case the UrQMD simulations—are based on the description of single particle-particle interactions

and nonequilibrium will be the normal case. Consequently, we have to account for these deviations from equilibrium in such a manner that we can reliably apply equilibrium spectral functions to calculate the emission of photons and dileptons.

In general it is difficult to really determine to which degree a system has reached equilibrium. Basically there are two dominant effects, which may serve as indicators for thermal and chemical equilibration: The momentum-space anisotropies and the appearance of meson-chemical potentials.

1. Thermal nonequilibrium

Regarding thermal equilibration, it was found in microscopic simulations that independent of the collision energy the system needs a time of roughly 10 fm/c after the beginning of the heavy-ion collision until the transverse and longitudinal pressures are approximately equal [56]. The pressure anisotropy stems from the initial strong compression along the beam axis when the two nuclei first hit and traverse each other. Because thermal equilibrium requires isotropy, one will obtain excessively high values for the energy density in highly anisotropic cells. To obtain effective quantities that account for the thermal properties in the system we apply a description that explicitly includes the momentum-space anisotropies and in which the energy-momentum-tensor is assumed to take the form [57,58]

$$T^{\mu\nu} = (\varepsilon + P_\perp)u^\mu u^\nu - P_\perp g^{\mu\nu} - \left(P_\perp - P_\parallel\right)v^\mu v^\nu, \qquad (7)$$

where $P_\perp$ and $P_\parallel$ denote transverse or parallel pressure components, respectively; u^μ and v^μ are the cell's four-velocity and the four-vector of the beam direction, respectively. The effective energy density ε_{eff} is obtained via the generalized equation of state for a Boltzmann-like system of the form

$$\varepsilon_{\text{eff}} = \frac{\varepsilon}{r(x)}, \qquad (8)$$

where the relaxation function $r(x)$ and its derivative $r'(x)$ are defined by

$$r(x) = \begin{cases} \frac{x^{-1/3}}{2}\left(1 + \frac{x\,\text{artanh}\sqrt{1-x}}{\sqrt{1-x}}\right) \text{for } x \leqslant 1 \\ \frac{x^{-1/3}}{2}\left(1 + \frac{x\,\arctan\sqrt{x-1}}{\sqrt{x-1}}\right) \text{for } x \geqslant 1, \end{cases} \qquad (9)$$

and $x = (P_\parallel/P_\perp)^{3/4}$ denotes the pressure anisotropy.

As we have shown in our previous investigation at SPS energies [27], with this description the effective energy density deviates from the nominal one only for the very initial stage of the reaction (the first 1–2 fm/c), where the pressure components differ by orders of magnitude. Nevertheless, the effective energy density ε_{eff} allows us to calculate meaningful T and μ_{B} values for these cells. After the very initial collision phase, the differences still exist but have hardly any influence on the energy density, so that we can assume that these cells are in approximate local equilibrium.

2. Chemical nonequilibrium

Chemical equilibration is a more difficult problem, but one obvious deviation in microscopic models is the appearance of meson chemical potentials, especially for the case of pions because these are the most abundantly produced particles. Since the meson number is not a conserved quantity in strong interactions (in contrast to, e.g., the baryon number), meson chemical potentials can only show up if the system is out of chemical equilibrium. While pion chemical potentials are introduced in fireball models for the stage after the chemical freeze-out to obtain the correct final pion yields, in nonequilibrium transport models they intrinsically appear in the early stages of the reaction when a large number of pions is produced in many initial scattering processes [59]. At higher collision energies this mainly happens via string excitation. The pion (and kaon) chemical potentials have a large influence on the photon and dilepton production rates as an overpopulation of these meson states increases the reactions in many important channels, for example $\pi\pi \to \rho \to \gamma/\gamma^*$ [60].

To implement the nonequilibrium effects in the calculations, we extract the pion and kaon chemical potentials in the Boltzmann approximation as [61]

$$\mu_{\pi/K} = T \ln\left(\frac{2\pi^2 n}{gTm^2 \text{K}_2\left(\frac{m}{T}\right)}\right), \qquad (10)$$

where n denotes the cell's pion or kaon density and K_2 is the Bessel function of the second kind. The degeneracy factor g is 3 in the case of pions and 2 for kaons. Note that the Boltzmann approximation is in order here because the mesons in the transport model also account for Boltzmann statistics and no Bose effects are implemented. However, whereas for a Bose gas the chemical potential is limited to the meson's mass, in principle one can get higher values for μ_π or μ_K here in rare cases. Because such values are nonphysical, we assume that the maximum values to be reached are 140 MeV for μ_π and 450 MeV for μ_K.

D. Equation of state

Once the rest-frame properties of each cell are determined, an equation of state (EoS) is necessary to describe the thermodynamic system of the hot and dense matter in the cell under the given set of state variables, i.e., the (effective) local energy density and the local net densities of conserved charges (for the strong interactions considered here the baryon number is the relevant quantity). For the present calculations we apply a hadron-gas equation of state (HG-EoS) that includes the same hadronic degrees of freedom as the underlying transport model [62]. The EoS allows us to extract the temperature and baryochemical potential for an equilibrated hadron gas at a given energy and baryon density. It is similar to the result obtained for UrQMD calculations in a box in the infinite-time limit, when the system has settled to an equilibrated state.

However, in the FAIR-energy regime a purely hadronic description of the evolving hot and dense fireball will not be sufficient. Because the temperatures will exceed the critical temperature T_c, a transition from hadronic to partonic matter has to be implemented, and the dynamic evolution of the created quark-gluon plasma has to be considered. On the other hand, it is necessary to keep the EoS consistent with the underlying dynamics which is purely hadronic. In our previous study at SPS energies [27], we supplemented the

HG-EoS with a lattice equation of state [63] for temperatures above $T_c \approx 170$ MeV, in line with the lattice results. In the range around the critical temperature, the results of the HG-EoS and the lattice EoS match very well for $\mu_B \approx 0$, while significantly higher temperatures are obtained with the latter for $T \gg T_c$.

However, this procedure is problematic for the present study, because the transition from a hadronic to a partonic phase and back is assumed to take place at finite values of μ_B at FAIR energies, whereas the lattice EoS is restricted to vanishing chemical potential. To avoid discontinuities in the evolution, we confine ourselves to the application of the HG-EoS, but with the assumption that the thermal emission from cells with a temperature above 170 MeV stems from the QGP (i.e., we employ partonic emission rates). This should be in order, because the temperatures will not lie too much above the critical temperature at the energies considered in the present work. Here the deviations from a full QCD-EoS explicitly including a phase transition are expected to be rather moderate.

Nevertheless, we once again remind the reader that the underlying microscopic description is purely hadronic and it remains to be studied which consequences a phase transition has at the microscopic level of the reaction dynamics.

III. PHOTON AND DILEPTON RATES

The mechanisms which contribute to the thermal emission of photons and dileptons are the same. Any process that can produce a real photon γ can also produce a virtual (massive) photon γ^*, decaying into a lepton pair. However, due to the different kinematic regimes probed by photons and dileptons, the importance of the single processes varies. In the following the various sources of thermal radiation considered in this work are presented.

Determining quantity for the thermal emission of real photons as well as virtual photons (i.e., dileptons) is the imaginary part of the retarded electromagnetic current-current correlation function $\Pi_{\rm em}^{\rm (ret)}$, to which the rates are directly proportional. It represents a coherent summation of the cuts of those Feynman diagrams which describe the different processes contributing to thermal γ and γ^* emission, and therefore accounts for the photon or dilepton self-energy. In the rest frame, the thermal emission can be calculated according to [25]

$$\frac{dN_{ll}}{d^4x d^4q} = -\frac{\alpha_{\rm em}^2 L(M)}{\pi^3 M^2} f_{\rm B}(q;T) \times {\rm Im}\Pi_{\rm em}^{\rm (ret)}(M,\vec{q};\mu_B,T), \quad (11)$$

$$q_0 \frac{dN_\gamma}{d^4x d^3q} = -\frac{\alpha_{\rm em}}{\pi^2} f_{\rm B}(q;T) \times {\rm Im}\Pi_{\rm em}^{T,\rm (ret)}(q_0 = |\vec{q}\,|;\mu_B,T). \quad (12)$$

Here, $L(M^2)$ is the lepton phase-space factor (which plays a significant role only for masses close to the threshold $2m_l$ and is approximately unity otherwise), $f_{\rm B}$ is the Bose distribution function, and M is the invariant mass of a lepton pair. Note that only the transverse polarization of the current-current correlator enters for the photon rate, because the longitudinal projection vanishes at the photon point, i.e., for $M = 0$.

A. Thermal rates from hadronic matter

1. Vector meson spectral functions

In hadronic matter, all the spectral information of a hadron with certain quantum numbers is specified in ${\rm Im}\Pi_{\rm em}^{\rm (ret)}$ [64]. Assuming that vector meson dominance (VMD) [65] is valid, the correlator can be directly related to the spectral functions of vector mesons. The important challenge for theoretical models is to consider the modifications of the particle's self-energy inside a hot and dense medium. Different calculations of in-medium spectral functions exist [66–70]; however, not many of them fully consider the effects of temperature and finite chemical potential. In the present work we apply a hadronic many-body calculation from thermal field theory for the spectral functions of the ρ and ω mesons [71–73], which has proven to successfully describe photon and dilepton spectra from SIS 18 to LHC energies [20,22,27,28,45,74,75]. The calculation of the different contributions to the ρ spectral function takes three dominant effects into account: The modification due to the pion cloud and the direct scattering of the ρ with baryons (nucleons as well as excited N^* and Δ^* resonances) and with mesons $(\pi, K, \rho, \dots)$ [76]. While the pion-cloud effects also contribute in the vacuum, the scattering processes only show up in the medium. For the ω, the situation is slightly more complex since this meson basically constitutes a three-pion state. The vacuum self-energy is represented by a combination of the decays into $\rho + \pi$ or three pions, respectively. Furthermore, the inelastic absorption $\omega\pi \to \pi\pi$ and the scattering processes with baryons as well as the pion (i.e., $\omega\pi \to b_1$) are implemented [77]. In the same manner as in our previous dilepton study at SIS 18 energy [28], we relinquish a treatment of thermal emission from the ϕ vector meson here, for reason of the minor in-medium-broadening effects observed for this hadron and its still-low multiplicities, at least for lower FAIR energies. In the case of vanishing invariant mass, i.e., for real photons, only the ρ vector meson will give a significant contribution. For the present calculation, we used the parametrization of the photon rates from the ρ as given in Eqs. (2)–(7) in Ref. [78], while a more advanced parametrization is necessary for the dilepton rates from the ρ and ω, due to their dependence on invariant mass and momenta [79].

Note that, presently, the photon rate parametrization for the ρ contribution is limited to baryon chemical potentials lower than 400 MeV and momenta larger than 0.2 GeV/c. While we can easily neglect the lowest momentum region in the present study, the restriction to low μ_B is a problem for the lowest collision energies considered here, where one expects values of μ_B which significantly exceed this range. The difference will be dominant at lower momenta, where the influence of baryonic effects is known to be largest, while the effect of a finite chemical potential is rather small at higher momenta [78]. However, for the present work we can assume the photon contribution from the ρ meson as a lower limit with regard to the baryonic effects.

2. Meson-gas contributions

The contribution from vector mesons is not the only hadronic source of thermal emission. The mass region above the ϕ meson, i.e., for $M > 1$ GeV/c^2, is no longer dominated by well-defined particles, but one finds a large number of overlapping broad resonances constituting multimeson (mainly four-pion) states, which have a significant impact on the dilepton yield. Here, we apply a description relying on model-independent predictions using a low-temperature expansion in the chiral-reduction approach [74].

While the multimeson effects only show up for high invariant masses, i.e., in the timelike kinematic region probed by dileptons, when going to real photons with $M \to 0$ several scattering and bremsstrahlung processes become important, which can be mostly neglected at finite M. While baryonic bremsstrahlung processes such as $NN \to NN\gamma$ and $\pi N \to \pi N\gamma$ are included in the vector meson spectral functions, meson-meson bremsstrahlung has to be added in the case of photon emission. The most dominant part will here come from the meson-meson scatterings $\pi\pi \to \pi\pi\gamma$ and $\pi K \to \pi K\gamma$, for which we use the rates calculated within an effective hadronic model [23] in the form of the parametrization given by Eqs. (8) and (9) in Ref. [78]. Note that these bremsstrahlung processes are mainly contributing at low momenta, whereas they are rather subleading for photons of higher energy.

Besides the $\pi\pi$ and πK bremsstrahlung, also other mesonic reactions contribute to the thermal photon production, such as strangeness-bearing reactions and meson-exchange processes. In detail, these are $\pi\rho \to \pi\gamma$, $\pi K^* \to K\gamma$, $\pi K \to K^*\gamma$, $\rho K \to K\gamma$, and $K^*K \to \pi\gamma$ reactions. The corresponding thermal rates were calculated for a hot meson gas in Ref. [22], which are applied here together with the respective form factors.

Since the ω-t-channel exchange was found to give a significant contribution to thermal photon spectra via the $\pi\rho \to \pi\gamma$ process, it has been recently argued that other processes including a $\pi\rho\omega$ vertex should also be be considered in the calculations; namely, the $\pi\rho \to \gamma\omega$, $\pi\omega \to \gamma\rho$, and $\rho\omega \to \gamma\pi$ reactions for which the rates (including the form factors) are parametrized in Appendix B of Ref. [24]. Consequently, we also add these processes when calculating thermal photon spectra.

3. Influence of meson chemical potentials

As was already mentioned, we do not restrict ourselves to the consideration of emission from thermally and chemically equilibrated matter but also include nonequilibrium effects in the form of finite pion and kaon chemical potentials μ_π and μ_K. It has been shown in Ref. [25] that the influence of a nonequilibrium distribution of the respective mesons can be accounted for by introducing an additional fugacity factor

$$z^n_{M=\pi,K} = \exp\left(\frac{n\mu_M}{T}\right) \tag{13}$$

in the thermal dilepton and photon rates in Eqs. (11) and (12). The exponent n depends on the difference in pion or kaon number $N_{\pi/K}$ between initial and final state of the process, i.e., $n = N^i_{\pi/K} - N^f_{\pi/K}$. Note that, while the pion fugacity enters in most processes, the effects of a finite kaon chemical potential only play a role for the πK bremsstrahlung and $\pi + K^* \to \pi + \gamma$, $\pi + K \to K^* + \gamma$, and $K^* + K \to \pi + \gamma$ photon production channels. For the dilepton channels considered here, μ_K can be neglected.

TABLE I. Summary of the different dilepton contributions considered in the present calculations.

Type	Rates	Fugacity	Ref.
Dilepton	ρ (incl. baryon effects)	z_π^2	[73,79]
	ω (incl. baryon effects)	z_π^3	[73,79]
	Multipion	z_π^3 / z_π^4 / z_π^5	[45]
Photon	ρ (incl. baryon effects)	z_π^2	[73,78]
	$\pi\pi$ and πK Bremsstr.	$z_\pi^2 + 0.2 z_\pi z_K$	[22,78]
	$\pi\rho \to \gamma\pi$	z_π^3	[22]
	$\pi K^* \to K\gamma$	$z_\pi z_K$	[22]
	$\pi K \to K^*\gamma$	$z_\pi^2 z_K$	[22]
	$\rho K \to K\gamma$	z_π	[22]
	$K^*K \to \pi\gamma$	z_K	[22]
	$\pi\omega \to \gamma\rho$	z_π^4	[24]
	$\rho\omega \to \gamma\pi$	z_π^5	[24]
	$\pi\rho \to \gamma\omega$	none	[24]

While for the single mesonic channels the initial and final state are always well defined, several different types of processes are included in the ρ and ω spectral functions, especially processes with baryons. For the ρ, not only processes with an initial two-pion state of the type $\pi\pi \to \rho \to \gamma/\gamma^*$ are accounted for, but also reactions including only one or no pion as ingoing particle (e.g., $\pi N \to \Delta \to \gamma N$ or $NN \to \gamma NN$). However, as the correct fugacity depends on the initial pion number, one would obtain different enhancements for each channel. But as the different processes interfere with each other it is difficult to determine the exact strength of each channel and consequently one might hardly be able to account for some average enhancement factor. Instead we apply here a fugacity factor z_π^2 which would be correct for pure $\pi\pi$ annihilation processes. This can be interpreted as an upper estimate of the influence which the meson chemical potential might have on the thermal ρ emission rates. The same procedure is applied for the ω meson, where we assume a fugacity of z_π^3. Note that while the multipion contribution also accounts for different initial states, they are each treated separately so that one can apply the correct fugacity factors here.

A full list of all hadronic contributions considered for the present calculation of thermal dilepton and photon emission, including the corresponding fugacity factors which account for the enhancement of the specific channel due to the meson chemical potentials, is given in Table I.

B. Quark-gluon plasma

For the thermal emission of electromagnetic probes from the quark-gluon plasma one is again confronted with the problem that different processes govern the dilepton production on the one side and photon emission on the other. Consequently, one has to apply two different descriptions for thermal rates, which are presented in the following.

In case of photon emission from a partonic phase of quarks and gluons the two main contributions stem from quark-antiquark annihilation ($q\bar{q} \to g\gamma$) and Compton scattering processes ($qg \to q\gamma$ or $\bar{q}g \to \bar{q}\gamma$) [80]. However, it was shown that these processes are not sufficient to describe the production mechanism correctly and that it is necessary to (a) include Feynman diagrams accounting for bremsstrahlung and inelastic annihilation processes which are enhanced due to near-collinear singularities and (b) to implement the Landau–Pomeranchuk–Migdal effect [81,82]. The result of a full calculation of the photon emission, to leading order in $\alpha_{\rm em}$, and the QCD coupling $g(T)$ was evaluated by Arnold, Moore, and Yaffe and takes the following form [83]:

$$q_0 \frac{dR_\gamma}{d^3q} = -\frac{\alpha_{\rm em}\alpha_{\rm s}}{\pi^2} T^2 \left(\frac{5}{9}\right) f_{\rm B}(q;T) \times \left[\ln\left(\sqrt{\frac{3}{4\pi\alpha_{\rm s}}}\right) + \frac{1}{2}\ln\left(\frac{2q}{T}\right) + C_{\rm tot}\right], \quad (14)$$

with

$$C_{\rm tot} = C_{2\leftrightarrow 2}\left(\frac{q}{T}\right) + C_{\rm annih}\left(\frac{q}{T}\right) + C_{\rm brems}\left(\frac{q}{T}\right), \quad (15)$$

$$\alpha_{\rm s} \approx \frac{6\pi}{27\ln(T/0.022)}. \quad (16)$$

The functions $C_{2\leftrightarrow 2}$, $C_{\rm annih}$ and $C_{\rm brems}$ are approximated by the phenomenological fits given in Eqs. (1.9) and (1.10) in Ref. [83]. Note that this calculation assumes the chemical potential to be vanishing. However, the overall effect of finite values of a quark chemical potential (i.e., nonequal numbers of quarks and antiquarks in the QGP phase) is known to be rather small.

In case of the thermal dilepton emission from the QGP, the leading-order contribution is the electromagnetic annihilation of a quark and an antiquark into a virtual photon, $q\bar{q} \to \gamma^*$. This process is irrelevant in the light-cone limit for $M \to 0$, because the annihilation of two massive quarks into a massless photon is kinematically forbidden. The pure perturbative quark-gluon plasma rate was calculated for the mentioned leading-order process [84] as

$$\frac{dR_{ll}}{d^4p} = \frac{\alpha_{\rm em}^2}{4\pi^4}\frac{T}{p} f^{\rm B}(p_0;T) \sum_q e_q^2 \times \ln\frac{(x_- + y)(x_+ + \exp[-\mu_q/T])}{(x_+ + y)(x_- + \exp[-\mu_q/T])}, \quad (17)$$

with $x_\pm = \exp[-(p_0 \pm p)/2T]$ and $y = \exp[-(p_0 + \mu_q)/T]$. The quark chemical potential μ_q which shows up here is equal to $\mu_{\rm B}/3$. This calculation approximates the full QCD results quite well at high energies, but for soft processes of the order $g_{\rm s}(T)$, i.e., for dileptons with low masses and momenta, the one-loop calculation is not sufficient and hard-thermal-loop (HTL) corrections to the result as given in Eq. (17) have to be considered [85]. It was found that the rate for soft dileptons is then orders of magnitude larger than the simple leading-order calculation [26].

Recent calculations from thermal lattice QCD suggest an even stronger enhancement of the rates for low-mass dileptons [86]. These results, which are applied in the present work, have been extrapolated to finite three-momenta by a fit to the leading-order pQCD rates such that the correlation function takes the form [26]

$$-{\rm Im}\Pi_{\rm EM} = \frac{C_{\rm EM}}{4\pi} M^2 \left(\hat{f}_2(q0,q;T) + Q^{\rm tot}_{\rm LAT}(M,q)\right), \quad (18)$$

where

$$Q^{\rm tot}_{\rm LAT}(M,q) = \frac{2\pi\alpha_{\rm s}}{3}\frac{T^2}{M^2}\left(2 + \frac{M^2}{q_0^2}\right) \times K F(M^2) \ln\left[1 + \frac{2.912}{4\pi\alpha_{\rm s}}\frac{q_0}{T}\right], \quad (19)$$

with a form factor $F(M^2) = 4T^2/(4T^2 + M^2)$ and a factor $K = 2$ to better fit the full lQCD rates. Note that, in contrast to the pQCD result, the rate in Eqs. (18) and (19) is calculated for $\mu_q = 0$ only, because a calculation for finite chemical potential is still beyond the current lattice calculations.

C. Hadronic decay contributions

While we restrict the calculation of photon yields to the thermal contribution, since all decay photons from long-lived hadronic resonances are usually subtracted from the experimental results, a full description of the dilepton spectra requires us to also take the nonthermal contributions from the decay of pseudoscalar and vector mesons into account. We here follow the same procedures as in our previous work for SIS 18 energies. In detail, we determine the following nonthermal dilepton contributions:

(1) The Dalitz decays of the pseudoscalar π^0 and η mesons. To determine their contribution, we assume that each final-state particle contributes with a weight of $\Gamma_{M\to e^+e^-}/\Gamma_{\rm tot}$.
(2) The direct decay of the ϕ meson into a lepton pair. Because the lifetime of the ϕ is relatively short, we apply a shining procedure which takes absorption and rescattering processes inside the medium into account.
(3) Finally, we restricted the calculation of thermal dileptons to those cells where the temperature is larger than 50 MeV, as otherwise a thermal description becomes questionable. However, in principle one will of course also find ρ and ω mesons at lower temperatures. To account for this, in the mentioned cases we calculate a "freeze-out" contribution from the ρ and ω decays using the UrQMD results for these mesons.

For a more detailed description of the nonthermal hadronic contributions the reader is referred to Ref. [28]. We refrain from an extensive reproduction of the procedure here, because the cocktail contributions will not play a significant role in the present investigations.

IV. RESULTS

In the following we present the results of calculations with the coarse-graining approach for Au + Au collisions in the energy range of $E_{\rm lab} = 2A$–$35A$ GeV. We restrict the analysis to the 10% most central reactions because the medium effects

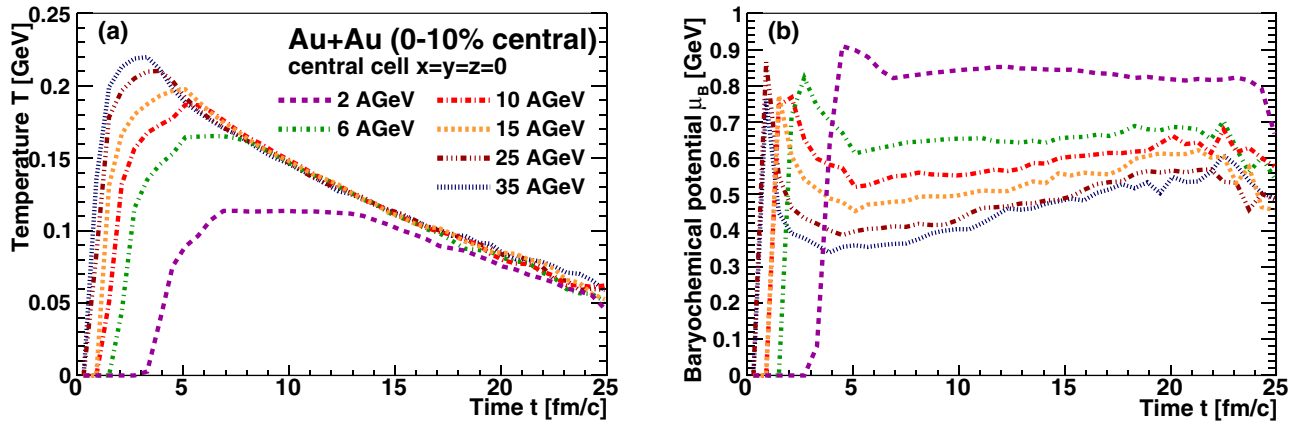

FIG. 1. Time evolution of (a) temperature T and (b) baryochemical potential μ_B for the central cell of the coarse-graining grid for different beam energies $E_{lab} = 2A$–$35A$ GeV. The results are obtained for the 0%–10% most central collisions in Au + Au reactions.

will be largest here. In terms of the microscopic UrQMD results, this roughly corresponds to an impact parameter range of $b = 0$–4.5 fm. For the coarse graining we use ensembles of 1000 microscopic events each. The length of the time steps is chosen as $\Delta t = 0.6$ fm/c, and the size of the spatial grid is $\Delta x = \Delta y = \Delta z = 0.8$ fm. These grid parameters are similar to those used for the previous studies at SIS 18 and SPS energies and constitute a good compromise between resolution and a sufficiently large hadron number per cell. To obtain enough statistics, especially for the nonthermal contributions, several runs with different ensembles are necessary.

A. Reaction dynamics

Because the dilepton and photon production is directly related to the space-time evolution of the thermodynamic properties of the system, it seems natural to start with a study of the reaction dynamics obtained with the coarse graining of the UrQMD input.

In Fig. 1 the time evolution of temperature and baryochemical potential in the central cell of the grid is depicted for different beam energies. The evolution shows a significant increase of the temperature maxima from slightly above 100 MeV for $2A$ GeV up to roughly 225 MeV for the top SIS 300 energy. While the temperature is clearly below the critical temperature of 170 MeV for the lower energies, the highest energies covered by FAIR can also probe this deconfinement region of the phase diagram. The thermal lifetime of the central cell, i.e., the time for which it rests at temperatures above 50 MeV, increases slightly with increasing collision energy. This is mainly due to an earlier onset of thermalization after the first hadron-hadron collisions, which define the origin of the time axis. However, it is interesting that, in the later phase of the collision, the temperature curves for all energies show the same monotonic decrease and even lie on top of each other. A somewhat different behavior is observed for the evolution of the baryochemical potential μ_B. For all energies it shows a clear peak with values between 700 and 900 MeV at the beginning of the collision, which is due to the high baryon densities reached in the central cell when the two nuclei first come into contact. Afterwards, μ_B decreases and then remains on a plateau level for a significant fraction of the reaction time for the lower energies, while one observes a slight increase for the higher beam energies towards later times. If we neglect the peak in the early reaction stage, the chemical potential shows a clear decrease with increasing collision energy. While for $2A$ GeV the baryochemical potential remains around 900 MeV for the whole thermal lifetime, μ_B is only 350 MeV at $t = 5$ fm for $35A$ GeV and slowly increases up to 600 MeV after $t = 20$ fm.

Note that the results shown in Fig. 1 are *only* for one single cell at the center of the collision. The evolution in other cells of the grid may differ largely in dependence on their location (e.g., one finds in general lower temperature and chemical potential in more dilute peripheral cells). But yet it clearly depicts the influence of collision energy on T and μ_B. One finds two effects when going from the lowest to the highest FAIR energies: An *increasing* temperature combined with a *decreasing* baryochemical potential. This behavior is not specific for the central cell but is reflected by the whole space-time evolution, as can be seen from Fig. 2. The two plots show the thermal four-volume as a function of temperature T (x axis) and baryochemical potential μ_B (y axis). Results are presented for $E_{lab} = 4A$ GeV [Fig. 2(a)] and $35A$ GeV [Fig. 2(b)]. We see that, for the lower energy, the largest part of the four-volume is concentrated at values of the baryochemical potential between 500 and 800 MeV, while the temperature remains below 160 MeV for all cells. In contrast, for $E_{lab} = 35A$ GeV the four-volume distribution extends to higher temperatures up to $T = 240$ MeV while at the same time the distribution is shifted to lower baryochemical potentials, especially for higher temperatures, while the lower-temperature cells are mainly dominated by high values of μ_B. Interestingly, especially for the higher collision energy of $35A$ GeV, one finds some cells in a separate region with moderate to high temperature and very low baryochemical potential $\mu_B \approx 0$. These cells are mainly found in the more peripheral regions of the collision, where the baryon density (and particle density in general) is rather low and where nevertheless in some cases hadrons with large momenta are found, resulting in high energy density for these cells. However, compared to the large overall total thermal volume, the relevance of these low-μ_B cells is negligible.

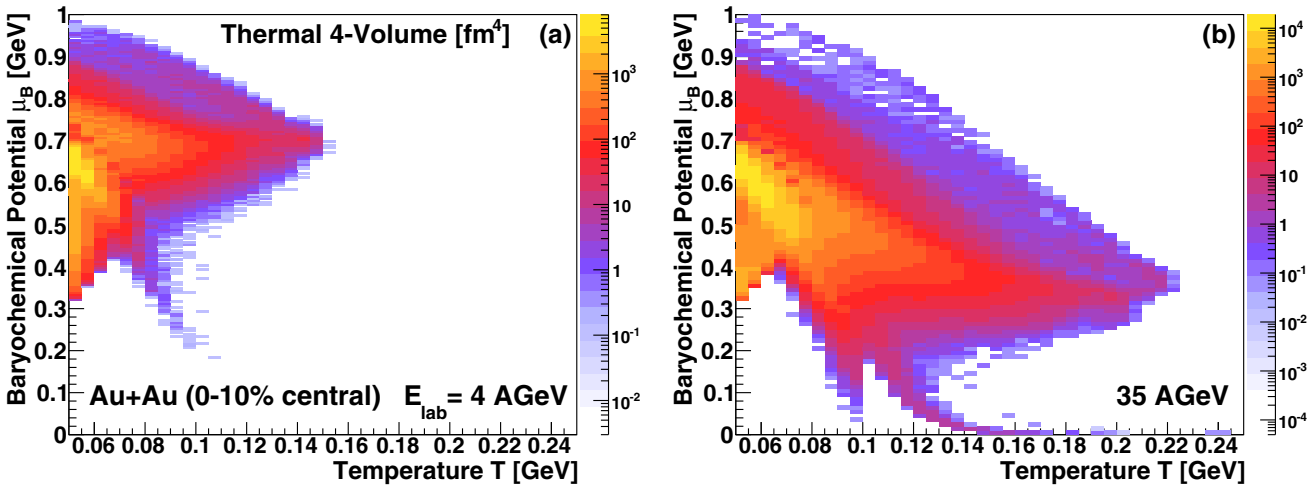

FIG. 2. Thermal four-volume in units of fm^4 from the coarse-grained transport calculations as a function of temperature T and baryochemical potential μ_{B}. Results are shown for (a) $E_{\mathrm{lab}} = 4A$ GeV and (b) $35A$ GeV in central Au + Au collisions.

It is important to bear in mind that the dilepton and photon spectra will directly reflect the four-volume evolution in the T-μ_{B} plane, as presented here. The results show that, at FAIR energies, the region of the QCD phase diagram with temperatures above the critical temperature *and* large μ_{B} can be probed, in contrast with the situation at the LHC or RHIC, where the transition from hadronic matter to a deconfined phase is assumed to happen at $\mu_{\mathrm{B}} \approx 0$. However, note that the present findings are obtained with a purely hadronic equation of state which does not include any effects of the phase transition itself. For an improvement of the description one might need to implement the transition properly to account, e.g., for the latent heat which would cause the cells to remain for a longer time at temperatures around T_{c}. Nevertheless, the present results can serve as a lower-limit baseline calculation, assuming that we have a smooth crossing from hadronic to QGP emission. Significant deviations from this assumption might then show up in the photon and dilepton spectra. We will discuss this later.

As was pointed out before, the effects of chemical nonequilibrium emerge in the form of finite meson chemical potentials for the π and K; and μ_π and μ_{K} can have a significant effect on the population of several photon and dilepton production channels. The mean values of the pion chemical potential μ_π and the kaon chemical potential μ_K as a function of the cell's temperature for different collision energies are shown in Fig. 3. Note that the results for the chemical potentials are obtained here by averaging the values of μ_π and μ_K over all space-time cells with a specific temperature. The study indeed indicates that, regarding the pion density, the system will be clearly out of equilibrium during the collision evolution. The value of μ_π increases with temperature, which is not surprising since a large part of the pion production in the microscopic simulation takes place in initial scatterings and via string formation at the beginning of the reaction, when the system still heats up. At all temperatures one finds that μ_π decreases with increasing collision energy, which may indicate a faster and stronger equilibration of the system if more energy is deposited in the system. In addition, for top SIS 300 energies the initial emission is dominated by QGP radiation at temperatures above T_c and consequently a larger fraction of cells with $T < 170$ MeV is found later in the course of the fireball evolution, when the system is in a more equilibrated condition compared with the very beginning of the collision. For the higher collision energies we get average values up to $\mu_\pi = 100$–120 MeV around the critical temperature of 170 MeV. Note that for $E_{\mathrm{lab}} = 4A$ GeV the maximum temperature found in the evolution is around 155 MeV, which explains the drop in the corresponding curve around this temperature.

In contrast to the large pion chemical potential, no such dominant off-equilibrium effect is observed for the kaons, where $\mu_K \approx 0$ at all energies and temperatures. This seems natural, because in the underlying microscopic simulations any inelastic reaction results in the creation of a π whereas the cross section for kaon production is rather low in the cases considered here (and especially for the lower FAIR energies). Consequently, the kaon production is a slow process

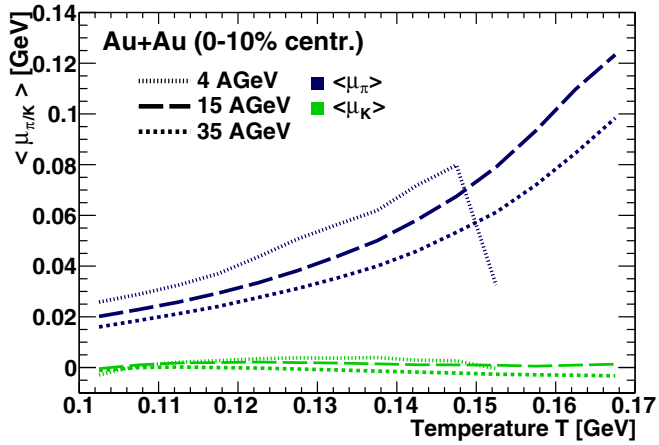

FIG. 3. Average values of the pion chemical potential μ_π (blue lines) and the kaon chemical potential μ_K (green lines) as a function of the cell temperature. Results are shown for central Au + Au collisions at three different collision energies, $E_{\mathrm{lab}} = 4A$, $15A$, and $35A$ GeV.

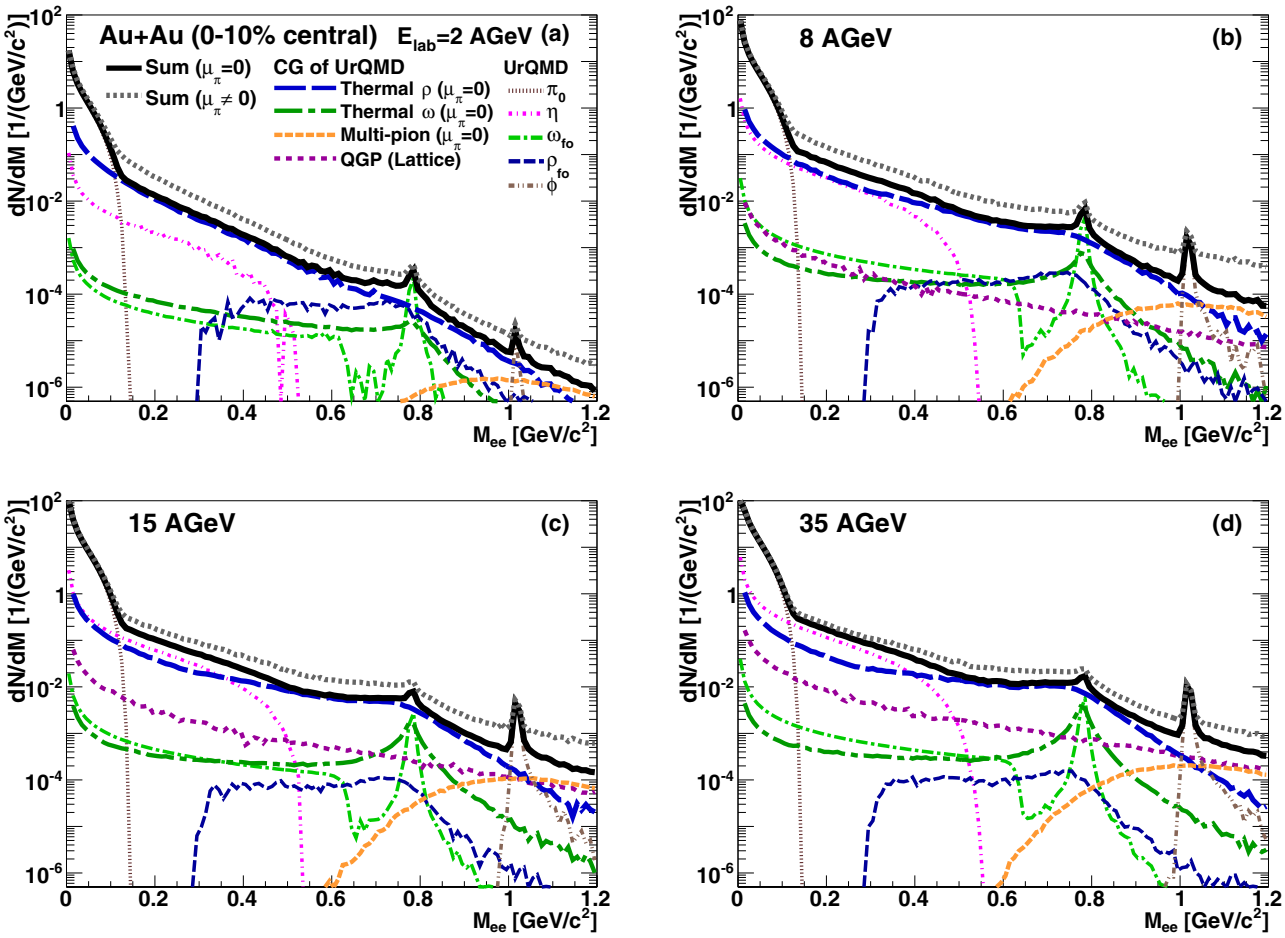

FIG. 4. Dilepton invariant-mass spectra for Au + Au reactions at different energies $E_{\rm lab} = 2A$–$35A$ GeV within the centrality class of 0%–10% most central collisions. The resulting spectra include thermal contributions from the coarse-graining of the microscopic simulations (CG of UrQMD) and the nonthermal contributions directly extracted from the transport calculations (UrQMD). The hadronic thermal contributions are only shown for vanishing pion chemical potential, while the total yield is plotted for both cases, $\mu_\pi = 0$ and $\mu_\pi \neq 0$.

which seems to happen synchronously with the equilibration of the system while a large amount of pions is produced in the initial hard nucleon-nucleon scatterings before any equilibration could take place.

The present results for the pion chemical potential are quite different from other model descriptions. For example, in fireball parametrizations the particle numbers are fixed at the chemical freeze-out of the system and consequently meson chemical potentials develop when the system cools down. However, this is just an *ad hoc* assumption in such models, as they are based on a presumed equilibrium within the system. In contrast, the overpopulation of pions is an intrinsic result stemming from the microscopic simulation in the case of the coarse-graining approach. Nevertheless, the very high pion chemical potentials in the temperature region close to the phase transition might be questionable, because one would assume that the transition from the quark–gluon plasma to a hadronic phase should produce a system where the mesons are in an equilibrium state. A fully satisfying description of the chemical off-equilibrium evolution is not feasible within the present approach and would require a microscopic and dynamical description of the phase transition and its underlying dynamics.

B. Dilepton spectra

The dilepton invariant-mass spectra in the low-mass range up to $M_{e^+e^-} = 1.2$ GeV/c^2 for four different beam energies ($E_{\rm lab} = 2A$, $8A$, $15A$, and $35A$ GeV) are presented in Fig. 4. The comparison shows some interesting similarities and differences: While the very low masses up 0.15 GeV/c^2 are generally dominated by the Dalitz decays of neutral pions, the region beyond the Dalitz peak up to the pole masses of the ρ and ω mesons (i.e., $\approx$770 MeV/c^2) is dominated by a strong thermal ρ contribution. The thermal yield shows an absolute increase with $E_{\rm lab}$, but its importance decreases relative to the nonthermal η yield. This means that the thermal low-mass enhancement of the dilepton yield above a hadronic vacuum cocktail decreases with increasing collision energy. This observation is explained by the decrease of the baryon chemical potential at higher collision energies, as has been mentioned in the previous section. In contrast, the increasing temperature leads to a significantly flatter shape of, especially, the ρ distribution in the invariant-mass spectrum. While for low energies the thermal yield decreases strongly when going to higher invariant masses, at the top FAIR energies this effect is less prominent and the population of high masses is enhanced.

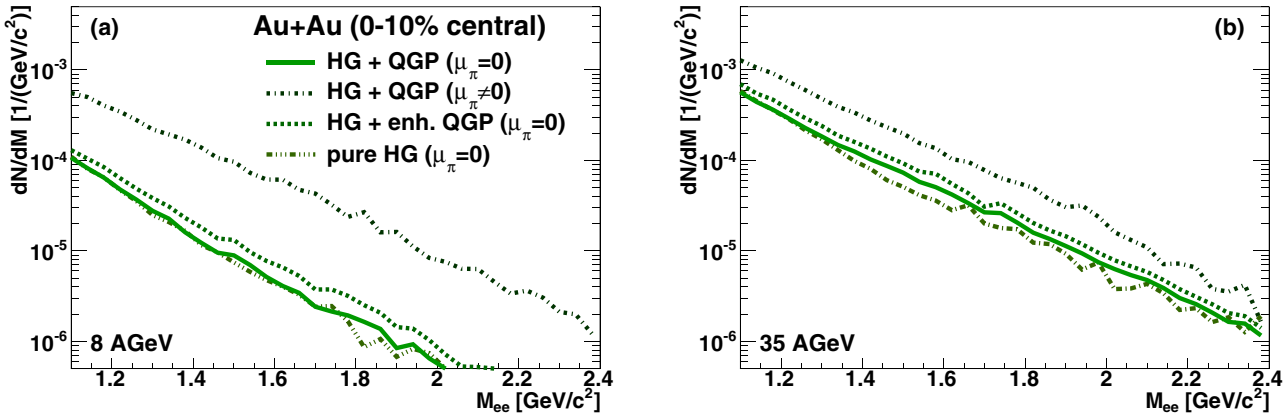

FIG. 5. High-mass region of the dilepton $M_{e^+e^-}$ spectrum for central Au + Au collisions at (a) $E_{\rm lab} = 8A$ GeV and (b) $35A$ GeV, assuming different emission scenarios. The baseline calculation assumes hadronic emission up to 170 MeV with vanishing μ_π and partonic emission for higher temperatures (full line). Besides the results with a five-times-enhanced emission around the critical temperature (dashed line) and for a pure hadron-gas scenario with emission at all temperatures from hadronic sources (dashed-triple-dotted line) are shown. Again, we also depict the baseline result including finite pion chemical potential (dashed-dotted line).

This can be clearly seen by the fact that the multipion yield shows a strong rise.

While at the lowest of the four energies the whole system is well below the critical temperature $T_{\rm c}$, we know from the temperature evolution in Fig. 1(a) that the region around $T \approx 170$ MeV is reached from $E_{\rm lab} = 6A$–$8A$ GeV on. In the dilepton invariant-mass spectra of Fig. 4 the resulting QGP contribution is very small at $8A$ GeV, but even at $35A$ GeV the partonic yield is suppressed by roughly an order of magnitude compared with the leading contributions in the mass range up to 1 GeV/c^2.

The hadronic thermal yields in Fig. 4 are shown for the case of vanishing pion chemical potential. However, we also compare the result for $\mu_\pi = 0$ with the total yield assuming finite values of μ_π. One can see that chemical nonequilibrium can increase the overall dilepton yield in the low-mass range up to a factor of two. For the region above 1 GeV/c^2 the effect can be even larger because the fugacity factor enters the thermal rate with a power of four for the multipion contribution. It is important to bear in mind that this result should rather be seen as an upper estimate, because the approximation $\mu_\rho = 2\mu_\pi$ is only correct for the rate $\pi\pi \to \rho$, which represents only one of the many processes included in the ρ spectral function. Furthermore, because UrQMD has no intrinsic description of the phase transition, the pion chemical potential might be overestimated in vicinity of the critical temperature. Nevertheless, the results show that a deviation from pion equilibrium has a huge impact on the thermal dilepton rates.

Considering possible signatures for a phase transition and the creation of a deconfined phase, the low-mass region is rather unsuited due to the dominance of the hadronic cocktail contributions and hadronic thermal emission from the vector mesons. Consequently, it might be more instructive to explore the mass range above the pole mass of the ϕ, where one has a continuum dominated by thermal radiation. In this region the hadronic cocktail contributions can be neglected and thermal sources will dominate the spectrum. In previous works [27,45] it was shown for SPS energies that the dilepton invariant-mass spectrum at very high masses $M_{l^+l^-} > 1.5$ GeV/c^2 could only be explained by including thermal radiation from the quark-gluon plasma. In Fig. 5 the higher-invariant-mass region for $M_{e^+e^-} > 1.1$ GeV/c^2 is shown for the two collision energies $E_{\rm lab} = 8A$ and $35A$ GeV. Here we compare four different scenarios to study whether the high-mass invariant-mass spectrum might help to identify the creation of a quark-gluon plasma. Besides the two standard scenarios (hadron gas + partonic emission above $T_{\rm c} = 170$ MeV) for (i) finite and (ii) vanishing μ_π, we include a scenario with (iii) a five-times-enhanced emission from the partonic phase around the transition temperature to simulate the effect of a critical slowdown of the system due to a first-order phase transition and, finally, (iv) a pure-hadron-gas scenario, where we assume all thermal radiation (also for $T > 170$ MeV) to stem from hadronic sources. For (iii) and (iv) $\mu_\pi = 0$ is assumed, too. The comparison shows that the spectral shape of the total yield is very similar for all scenarios, at both energies considered here. While the results for a purely hadronic scenario and including QGP emission from temperatures above $T_{\rm c}$ give quite the same results within 10% deviation, the artificially enhanced QGP emission also does not significantly increase the overall yield. In contrast, one observes a very strong enhancement due to a finite pion chemical potential, which shows up in our calculation by an overall increase by a factor of five at $8A$ GeV and still a factor of two at $35A$ GeV. The results indicate that it will be difficult to draw unambiguous conclusions from single measurements of the higher-mass region at a specific energy because, according to our calculations, a stronger QGP yield and less hadronic contribution can finally result in the same overall dilepton spectrum. Furthermore, the nonequilibrium effects may lead to much larger modifications of the spectrum than caused by the dynamics of the phase transition.

The transverse-momentum spectra, plotted for two different energies in different invariant-mass bins in Fig. 6, underline the previous finding. Again the slopes of the curves for hadronic and partonic emission are very similar for high masses,

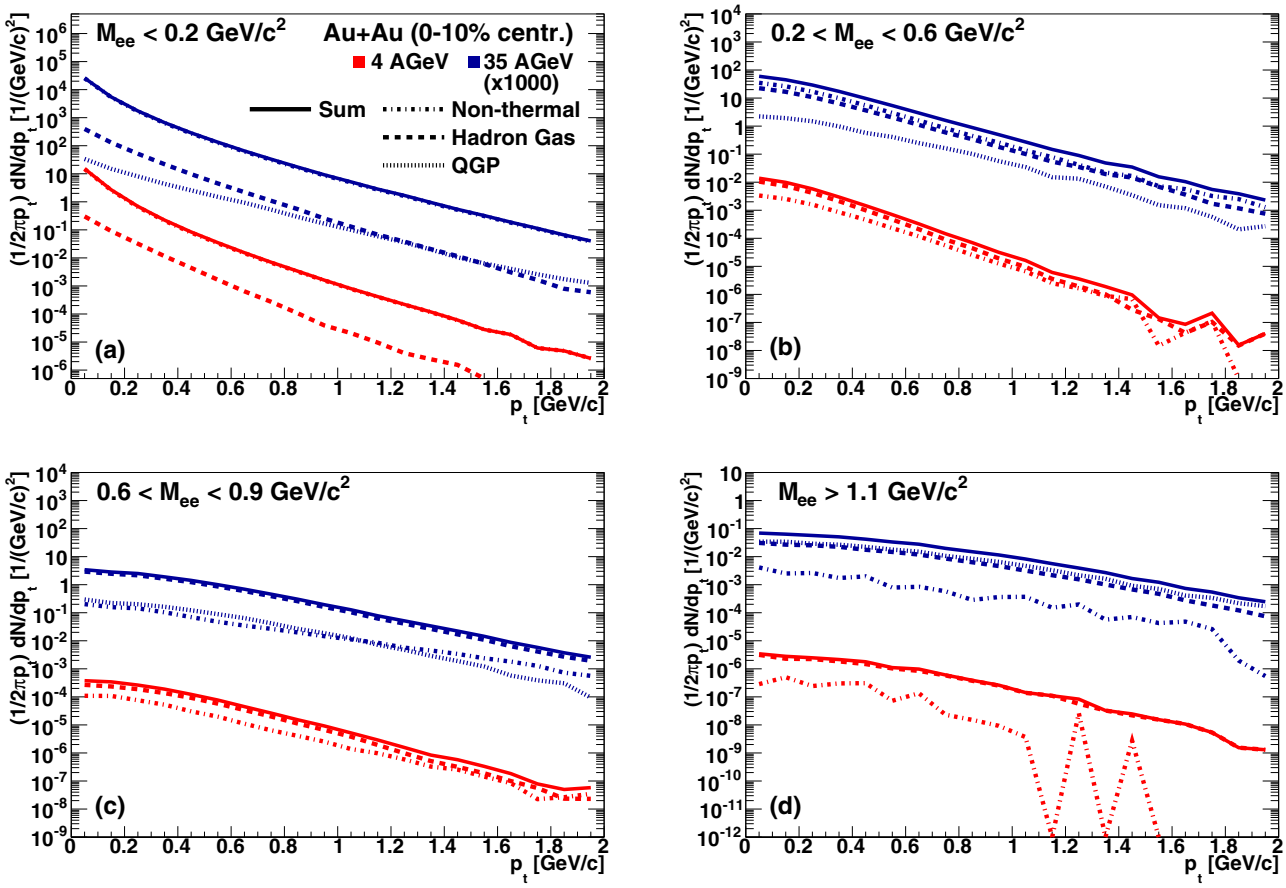

FIG. 6. Transverse-momentum spectra of the dilepton yield in central Au + Au reactions $E_{\rm lab} = 4A$ GeV (red) and $35A$ GeV (blue). The results are shown for four different invariant-mass bins: (a) $M_{e^+e^-} < 0.2$ GeV/c^2, (b) $0.2 < M_{e^+e^-} < 0.6$ GeV/c^2, (c) $0.6 < M_{e^+e^-} < 0.9$ GeV/c^2, and (d) $M_{e^+e^-} > 1.1$ GeV/c^2.

especially for $M_{e^+e^-} > 1.1$ GeV they are virtually identical. On the contrary, we find the partonic contribution to be harder (i.e., having a stronger relative yield at high transverse momenta) than the hadronic contribution in the lower mass bins. Together with the very similar invariant-mass spectra in Fig. 5 obtained with and without a partonic phase in the reaction evolution, the result confirms previous studies which showed a duality of emission rates in the transition-temperature region for high masses and momenta [26]. However, note that this is no longer true if one goes to a temperature regime significantly above $T_{\rm c}$. For this case clear differences between the hadronic and the partonic emission are observed. Unfortunately, even at the top SIS 300 energy only few cells reach temperature maxima above 200 MeV and one will not see clear differences between the partonic and hadronic emission patterns even at high $p_{\rm t}$ and high $M_{e^+e^-}$.

The reason for the duality showing up only at high invariant masses (and momenta, respectively) is twofold: On the one hand, the low-mass region is governed by the vector mesons with their specific spectral shapes and the baryonic effects on them. This effect has been called the "duality mismatch" [25] since the hadronic rates show an increase for finite baryochemical potentials, while the partonic emission rates are quite insensitive with regard to μ_q. On the other hand, while the spectra at low masses and momenta are populated by thermal emission at all temperatures, the production of dileptons for masses above 1 GeV/c^2 and for higher values of $p_{\rm t}$ is strongly suppressed at low temperatures. This is visible from Fig. 7(a), where the temperature-dependent dilepton yield from thermal sources for Au + Au at $E_{\rm lab} = 35A$ GeV is shown for different invariant-mass bins. (Note that the nonthermal lepton pairs directly extracted from the hadronic cocktail as calculated with UrQMD are not included here.) The yields shown in this plot represent the sum of the contributions from all cells at a certain temperature. While for the lowest mass bin $M_{e^+e^-} < 0.2$ GeV/c^2 the total thermal dilepton yield is built up by roughly equal fractions stemming from the whole temperature range, with slight suppression of emission from temperatures above $T_{\rm c}$, one can see that the mass region above $M_{e^+e^-} = 1.1$ GeV/c^2 is dominated by emission from temperatures between 140 to 220 MeV, which is exactly the assumed transition region between hadronic and partonic emission. Dilepton emission at lower temperatures is strongly suppressed in this mass range. Furthermore, one finds a smooth behavior of the thermal emission in the highest mass bin, but at lower masses one observes a slight kink in the rates at $T_{\rm c} = 170$ MeV. The finding indicates that, for lower masses, the partonic and hadronic rates do not perfectly match, as was discussed above. Another observation is the dominance of emission from the temperature range $T = 100$–140 MeV

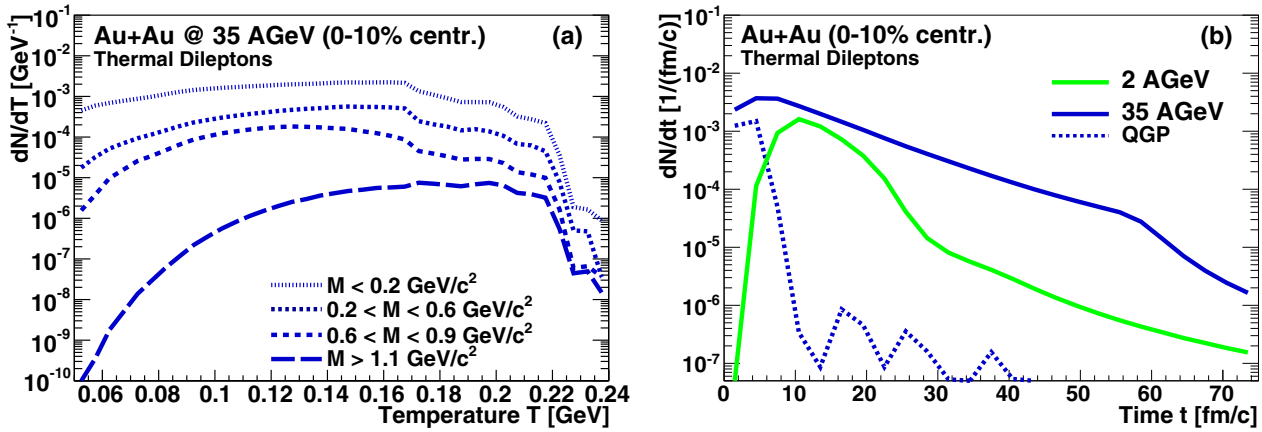

FIG. 7. (a) Temperature dependence of dilepton emission dN/dT from thermal sources for central Au + Au at $E_{\rm lab} = 35A$ GeV, i.e., the lepton pairs directly extracted from the hadronic cocktail as calculated with UrQMD are not included. The results are shown for four different invariant-mass bins: $M_{e^+e^-} < 0.2$ GeV/c^2, $0.2 < M_{e^+e^-} < 0.6$ GeV/c^2, $0.6 < M_{e^+e^-} < 0.9$ GeV/c^2, and $M_{e^+e^-} > 1.1$ GeV/c^2. (b) Time evolution dN/dt of thermal dilepton emission for $2A$ GeV (green) and $35A$ GeV (blue). The dashed line shows the emission from the QGP for the top FAIR energy.

for the mass region from 0.6 to 0.9 GeV/c^2. This result is in contrast to the general trend of a shift of the emission to higher temperatures when going to higher masses. However, the very mass region covers the pole masses of the ρ and ω meson. As the peak structures show a melting especially for finite baryon densities, one will get the largest yields in this mass range from cells for which $\mu_{\rm B} \approx 0$. A comparison with the T-$\mu_{\rm B}$ distribution of the cells at this energy in Fig. 2(b) shows that the largest fraction of cells for which the baryochemical potential is below 200 MeV lies exactly in the temperature range from 100 to 140 MeV.

Finally, it is instructing not only to look at the temperature but also at the time dependence of thermal dilepton emission as presented in Figure 7(b). The total dilepton emission per time step dN/dt as the sum from all cells is shown for $E_{\rm lab} = 2A$ and $35A$ GeV. In principle, the results reflect the findings from Fig. 1 and are similar to the temperature evolution depicted there. The system shows a faster heating for the top SIS 300 energy with higher temperatures, resulting in a larger number of emitted dileptons; partonic emission from cells with $T > T_c$ is found for the first 5–10 fm/c and only very sporadically thereafter. At lower energies the evolution is retarded and T remains below the critical temperature. However, in contrast to the slow heating of the system (which is simply due to the fact that the nuclei are moving slower) the thermal emission drops much earlier for $2A$ GeV (compared to $35A$ GeV) and only few cells with thermal emission are found for $t > 30$ fm/c. The higher energy deposited in the system with increasing $E_{\rm lab}$ obviously results not only in higher initial temperatures, but also in an enhanced emission at later stages, as it takes the system longer to cool down. Interestingly, for both energies one finds some sparse cells with thermal emission even after 60–70 fm/c; however, their contribution to the overall result is suppressed by three to four orders of magnitude compared with the early reaction stages.

C. Photon spectra

While we have two kinematic variables (momentum and invariant mass) which can be probed for virtual photons, real (i.e., massless) photons only carry a specific energy. In this

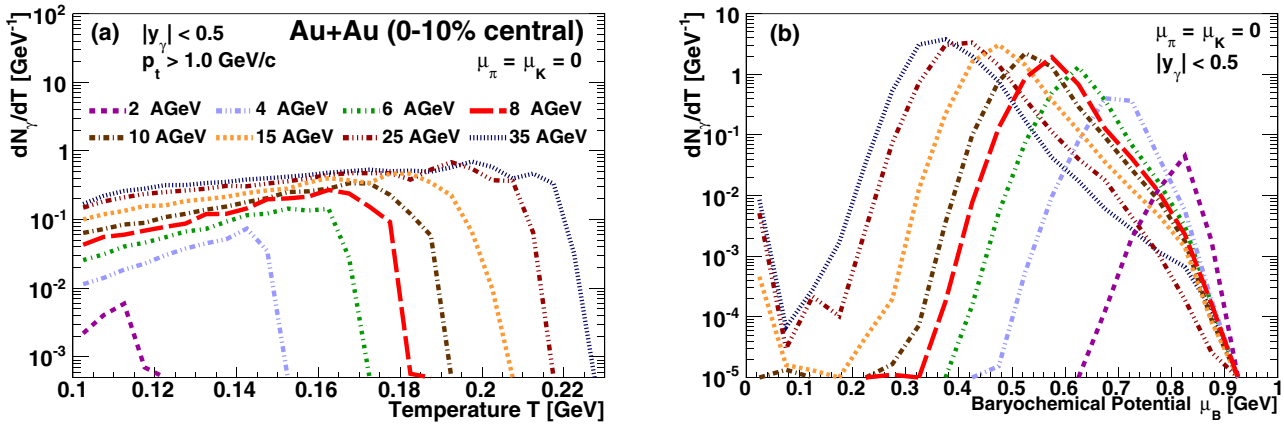

FIG. 8. Thermal photon yield at midrapidity in dependence on (a) temperature, dN_γ/dT, and (b) baryochemical potential, $dN_\gamma/d\mu_{\rm B}$, for central Au + Au collisions at different beam energies $E_{\rm lab} = 2A$–$35A$ GeV. The results are shown for the case of vanishing μ_π and $\mu_{\rm K}$.

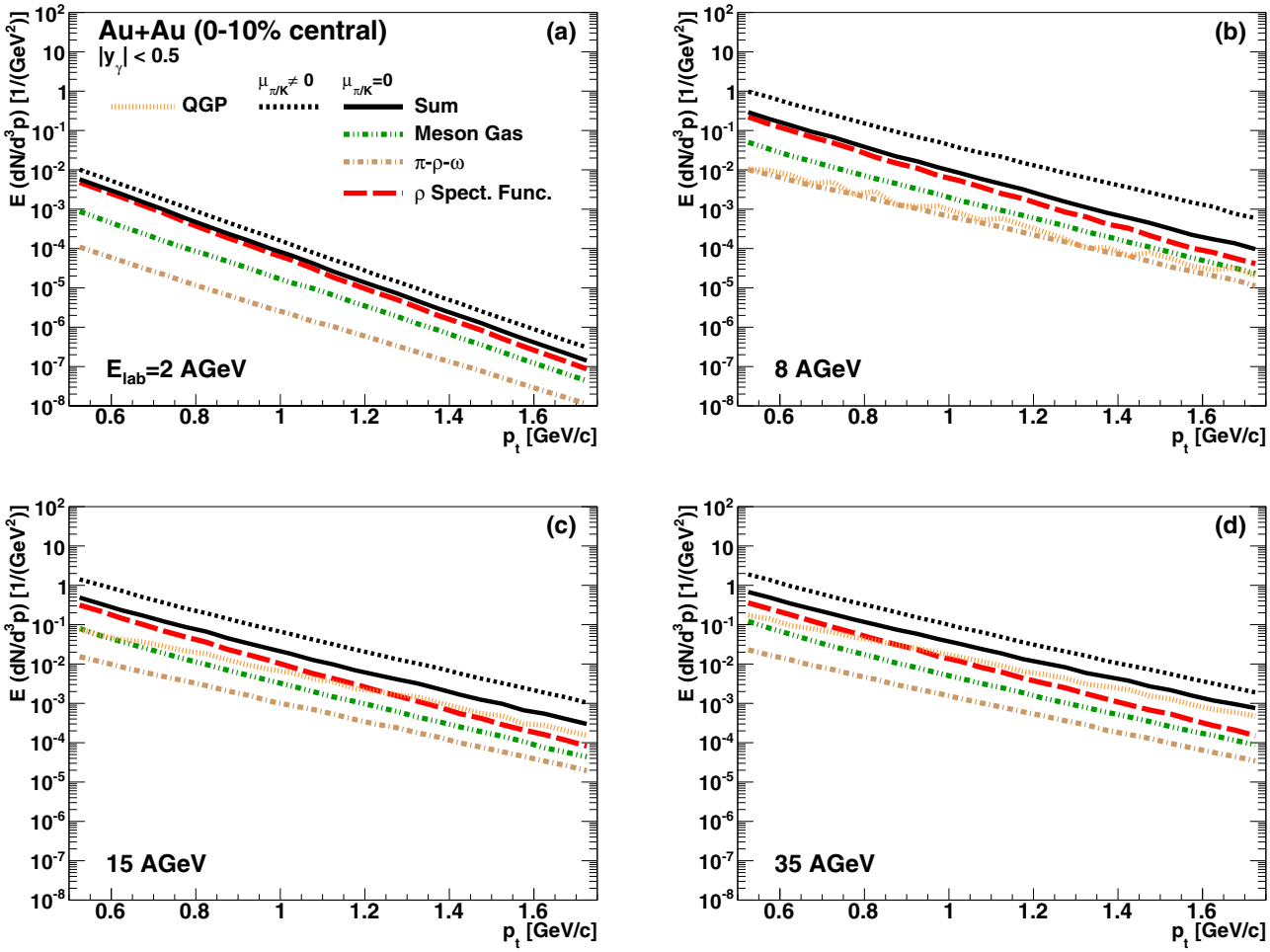

FIG. 9. Transverse-momentum spectra at midrapidity ($|y_\gamma| < 0.5$) of the thermal photon yield for central Au + Au reactions at (a) $E_{\rm lab} = 2A$ GeV, (b) $8A$ GeV, (c) $15A$ GeV and (d) $35A$ GeV. The total yields are plotted for both cases $\mu_\pi = 0$ (full black line) and $\mu_\pi \neq 0$ (dashed line). The single hadronic contributions from the ρ spectral function (red, long dashed), the meson gas (green, dashed-double-dotted), and the π-ρ-ω complex (beige, dashed-dotted) are only shown for vanishing pion chemical potential. The partonic contribution from the QGP is plotted as orange short-dashed line.

sense, dileptons are the more versatile probes of the hot and dense medium and carry additional information, especially regarding the spectral modifications of the vector mesons. Nevertheless, the correct description of the experimental photon spectra has been a major challenge for theory at SPS and RHIC energies. In the kinematic limit $M \to 0$ several processes become dominant which are negligible in the time-like region probed by dileptons, as was discussed in Sec. III. Consequently, the study of photon production can provide complementary information for the theoretical description of thermal emission rates and the reaction dynamics.

Because the parametrized photon emission rates have some restrictions with regard to the $\mu_{\rm B}$ range of their applicability, it will be instructive to find out at the beginning under which thermodynamic conditions the photons are emitted at FAIR. Figure 8 shows the dependence of thermal photon emission (at midrapidity) on temperature in the left plot [Fig. 8(a)] and on baryochemical potential in the right plot [Fig. 8(b)]. As in Fig. 7, the yields are the sum of the thermal contributions from all cells with a certain temperature or baryochemical potential, respectively. For both results we consider the case of vanishing meson chemical potentials. Note that, for the temperature dependence, we consider only the thermal emission at higher transverse momentum values $p_t > 1$ GeV/c, because here the duality between hadronic and partonic rates should be approximately fulfilled, which is indeed visible from the continuous trend of the thermal photon emission around $T_{\rm c}$. One can see that, especially for lower collision energies, the thermal emission is dominated by the cells which reach the maximum temperature, whereas the curves become flatter at higher energies. Even at the top energy of $35A$ GeV with maximum temperatures above 220 MeV still a significant amount of emission also stems from the cells with temperatures around 100 MeV.

Regarding the photon emission related to baryochemical potential as presented in Fig. 8(b), a clear energy-dependent trend is visible: While at low energies the largest fraction of emission stems from cells with very high values of $\mu_{\rm B}$ around 900 MeV, the emission-weighted average chemical potential drops continuously to 300–400 MeV at $35A$ GeV.

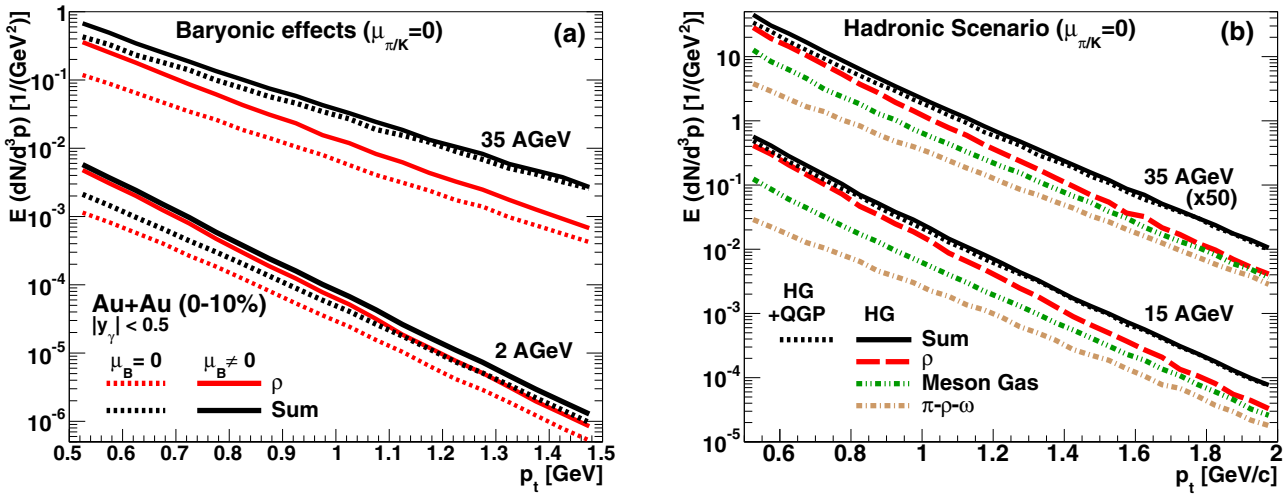

FIG. 10. Comparison of the transverse-momentum spectra at midrapidity ($|y_\gamma| < 0.5$) of the thermal photon yield for central Au + Au reactions resulting from different emission scenarios. In panel (a) the effect of a finite baryon chemical potential μ_B on the transverse momentum spectrum for the ρ contribution and the total yield is shown for $2A$ GeV (lower results) and $35A$ GeV (upper results), comparing the standard scenario with $\mu_B \neq 0$ (full lines) with the results for $\mu_B = 0$ (dashed lines). Panel (b) shows the results for a purely hadronic scenario, i.e., for emission from the hadron gas also for $T > 170$ MeV and no partonic contribution. The single contributions are plotted as in Fig. 9; for comparison the total yield for the standard result including hadronic + partonic emission is shown (black dashed).

However, the emission from cells with higher values of the baryochemical potential is by far not negligible. In consequence, the findings once again underline that the strongest baryonic modifications of the spectral functions will be present at low energies. The results also show that to fully account for the baryonic effects on the photon emission the spectral functions should be able to reliably cover the whole μ_B region from 0 to the nucleon mass (i.e., ≈900 MeV). The presently used parametrization will provide only a lower limit for the photon yield, especially for the lower collision energies.

In Figs. 9(a)–9(d) the transverse-momentum spectra of thermal photons for four different collision energies are presented. As for the dilepton invariant-mass spectra, we show the results without (full black line) and with (dashed black line) meson chemical potentials; once again the two calculations provide a lower and upper boundary for the off-equilibrium influence on the thermal yields, respectively. Two observations can be made when comparing the results for the different energies: An overall increase of the photon yield with increasing energy and, second, a simultaneous hardening of the spectra, i.e., one gets a stronger relative contribution for higher momenta. This is similar to the dilepton invariant-mass spectra, where the yield in the higher-mass region is suppressed for lower collision energies due to the lower overall temperatures in the fireball. (A more explicit comparison of the energy dependence of the results will be undertaken in Sec. IV D). Furthermore, one can see that, at all energies, the contribution from the ρ meson dominates above the other hadronic contributions especially for low p_t, while the relative dominance of the ρ decreases for higher momenta. The contribution from the quark-gluon plasma is visible for $E_{lab} = 8A$ GeV and higher energies, giving an increasing fraction of the overall yield. Note the similarity between the low-mass dilepton and photon p_t spectra for $35A$ GeV: In both cases the slope of the (virtual or real) photons emitted from the QGP stage is significantly harder than the contribution from hadronic sources. Furthermore, looking only at the ρ and the partonic contribution, one finds that the former is stronger for $p_t < 1$ GeV/c, and the latter dominates for higher momenta—for both dileptons and photons. This behavior is expected as the real photon represents just the $M_{e^+e^-} \to 0$ limit of virtual photon production. This is another requirement of consistency for the thermal rates.

Although finite values of μ_π and μ_K have an even more pronounced effect on the photon rates than on the dilepton rates, because several processes to be considered are very sensitive to an overpopulation of pions, it is remarkable that the overall effect leaves the shape of the photon p_t spectra mostly unchanged: The yields are enhanced by the same factor at all transverse momenta. This is interesting because the effect of $\mu_{\pi/K} \neq 0$ on the different contributions is varying in strength. For example, the yield from the π-ρ-ω system shows a much stronger enhancement than the ρ contribution (compare Table I).

But not only meson chemical potentials influence the photon spectra, similar to the case of dileptons, one also expects an enhancement of the ρ contribution in the presence of baryonic matter. In Fig. 10(a) the effect of a finite baryon chemical potential μ_B on the transverse momentum spectrum for the ρ contribution and the total yield is shown for $2A$ GeV and $35A$ GeV, comparing the standard scenario with $\mu_B \neq 0$ (full lines) with the results for $\mu_B = 0$ (dashed lines). The comparison shows that, especially at lower momenta, the ρ contribution is significantly increased for finite baryochemical potential, while this effect is less dominant at larger p_t. Furthermore, the effect is stronger for lower collision energies, where one obtains larger average values of μ_B. However, one should bear in mind that the parametrization for the

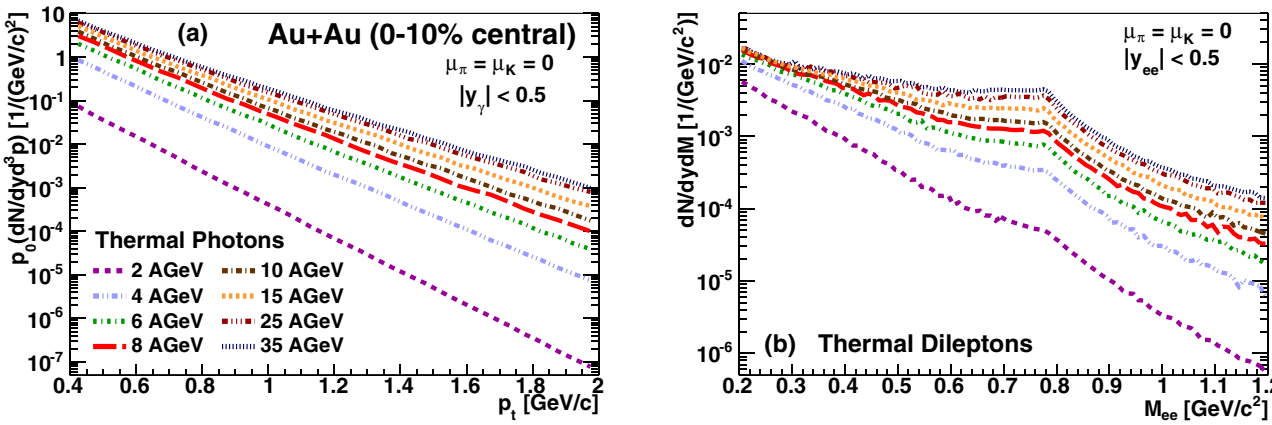

FIG. 11. (b) Comparison of the overall photon transverse-momentum spectra and (b) the thermal dilepton invariant-mass spectra at midrapidity $|y| < 0.5$ for different energies in the range $E_{\rm lab} = 2A$–$35A$ GeV. The results are shown for vanishing meson chemical potentials $\mu_\pi = \mu_K = 0$.

photon emission rates is limited to chemical potentials below 400 MeV, so that one cannot fully account for the very large chemical potentials in this case. In consequence, one can expect an even larger enhancement in the experimental measurements than in the present calculation.

To conclude the study of the different influences on the photon spectra, we also consider whether the possible creation of a deconfined phase has any effect on the thermal emission pattern. Figure 10(b) shows the results for a purely hadronic scenario, i.e., for emission from the hadron gas also for $T > 170$ MeV and no partonic contribution. For comparison also the total yield for the standard scenario including hadronic + partonic emission is shown. (For both cases the meson chemical potentials are assumed to be zero.) Again, as for the high-mass dileptons (compare Fig. 5), the differences between the two scenarios are negligible, especially compared to the effect of the meson and baryochemical potentials. Only a very slight enhancement of the yield at low momenta is obtained for the pure-hadron-gas scenario, reflecting the different sensitivity of partonic and hadronic rates to finite $\mu_{\rm B}$.

D. Excitation function of photon and dilepton yields

In the previous sections several differences and similarities between dilepton and photon spectra have already been discussed. However, it is instructing to do this in more detail and to compare the energy dependence of the emission patterns for photons and dileptons. Considering experimental measurements, an advantage of studying the excitation function of thermal yields might be that the trends and results obtained hereby at different energies are more robust and less sensitive to errors of measurement. It reflects the results of several different measurements in contrast to single spectra at a specific energy. For reasons of comparison and because the baryonic effects are strongest in this case, all results in the following will be considered for midrapidity $|y| < 0.5$.

In Fig. 11 the total thermal photon $p_{\rm t}$ and dilepton $M_{e^+e^-}$ spectra for eight different collision energies in the range $E_{\rm lab} = 2A$–$35A$ GeV are shown. It was already mentioned that—besides the hadronic structures due to the direct connection of the dilepton spectrum with the spectral function of the light vector mesons—the two spectra are strikingly similar. Also, the change of the spectra with increasing collision energy is alike. At high masses or momenta the yield shows a stronger increase with $E_{\rm lab}$ than in the low-mass or low-momentum region. More quantitatively, this can be seen in Fig. 12(a), where the relative increase of the thermal photon and dilepton yield for different transverse momentum or invariant-mass regions, respectively, is shown. The results are normalized to unity for $E_{\rm lab} = 2A$ GeV. One observes that the relative increase is stronger for high momenta and masses than for the lower-$p_{\rm t}$ or $M_{e^+e^-}$ bins. For example, the total dilepton yield for masses below 300 MeV/c^2 increases only by a factor of two from $E_{\rm lab} = 2A$ to $8A$ GeV and remains nearly constant thereafter, whereas in the high-mass region above 1 GeV/c^2 the yield increases by a factor 100 when going to the top SIS 300 energy of $35A$ GeV. A similar behavior is found for the photons, where the yield shows a more pronounced rise at high momenta. As was already pointed out before, one reason for this is the fact that much energy is needed to produce a dilepton at high mass or a photon with high momentum. Their production is strongly suppressed at the rather moderate temperatures obtained at lower collision energies. Note that, in general, the overall increase in the photon spectra is slightly stronger than for the dilepton production. This might be due to the limitation of the photon parametrization to temperatures above 100 MeV and baryochemical potentials below 400 MeV, which might somewhat underestimate the photon yield at the lowest collision energies. Besides, one should keep in mind that, in detail, the processes contributing to the thermal emission rates for dileptons and photons differ, which may also explain some differences between the results.

In contrast, we find that the fraction of the QGP yield compared to the total thermal emission is larger for the high-$M_{e^+e^-}$ dileptons compared to the high-$p_{\rm t}$ photons. The first significant QGP contribution is found for $E_{\rm lab} = 8A$ GeV, and the fraction continuously increases up to roughly 70% at $35A$ GeV for dilepton masses above 1 GeV/c^2 and 50% for photon momenta over 1 GeV/c. At lower masses or momenta, respectively, the hadronic contribution becomes

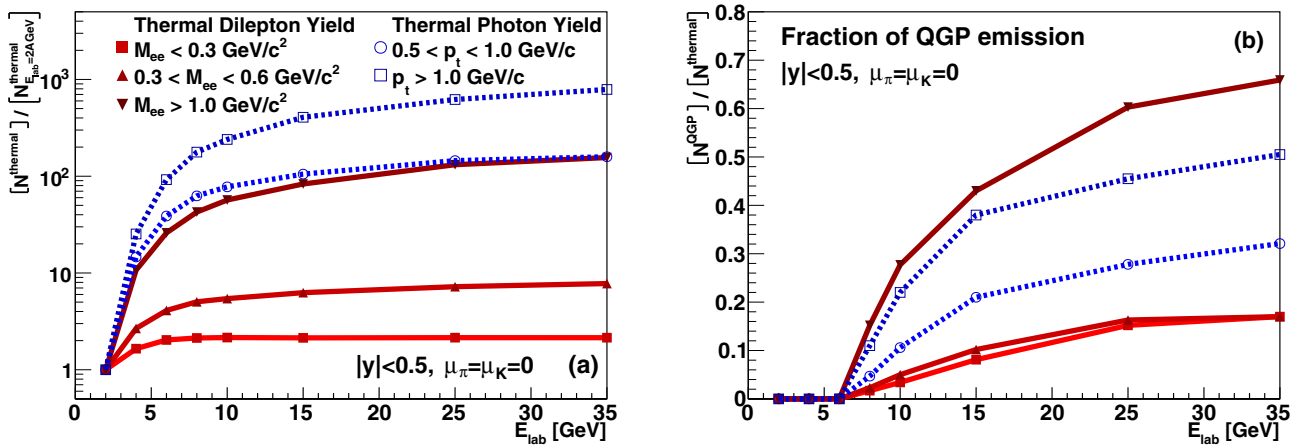

FIG. 12. (a) Energy dependence of the thermal photon and dilepton yield in different invariant-mass or transverse-momentum bins, respectively. The yields are normalized to the result at $E_{\rm lab} = 2A$ GeV. (b) Fraction of thermal QGP emission in relation to the total thermal yield of photons or dileptons in different $M_{e^+e^-}$ and photon-$p_{\rm t}$ bins. All results in this figure are shown for midrapidity and vanishing meson chemical potentials.

more dominant. This is not surprising, because one could already conclude that we probe lower temperatures at lower masses and momenta, compare Fig. 7(a). Furthermore, the baryonic influence increases here. The direct connection to the vector meson spectral functions makes the comparison difficult between the photon and dilepton results for low momenta and masses.

Finally, we consider also the thermal photon yield in relation to the number of (neutral) pions which are produced in the heavy-ion collision, as presented in Fig. 13. This ratio is of theoretical and experimental interest: For the experimental study of photons, decays of neutral pions are the major background in the analysis. On the theoretical side, the number of pions gives an estimate of the freeze-out volume and is not sensitive to the details of the reaction evolution. While the electromagnetic emission takes place over the whole lifetime of the fireball and therefore reflects the evolution of the system in the phase diagram, the pion yield allows us to scale cut trivial dependencies. Previously, the thermal dilepton yield was found to scale with $N_\pi^{4/3}$ if one compares different system sizes at SIS 18 energies [28]. However, the situation is more complex here because we consider a large range of energies, which will be covered by FAIR. Several effects play a role, e.g., the lifetime of the fireball, the temperatures and baryochemical potentials which are reached, and the different processes which contribute at different temperatures. While in our study at SIS 18 energies only the system size was modified (and all the other parameters could be assumed to remain quite constant, because one single energy was considered), in the present study *only* the size of the colliding nuclei is constant.

The investigation of the N_γ/N_{π^0} ratio is combined here with a comparison of the different scenarios for the conditions of thermal emission, which were already studied in the case of the photon and dilepton spectra (see Figs. 5 and 9). Varying $E_{\rm lab}$ (and, in consequence, T and $\mu_{\rm B}$) might result in distinct excitation functions of the ratio N_γ/N_{π^0} for the various scenarios, in contrast with the spectra for one specific energy where no unambiguous distinction was possible. In Fig. 13, one can see a strong increase of the photon-to-pion ratio with $E_{\rm lab}$ for the lowest energies, for both the lower-$p_{\rm t}$ range from 0.5 to 1 GeV/c and the high-transverse-momentum region above

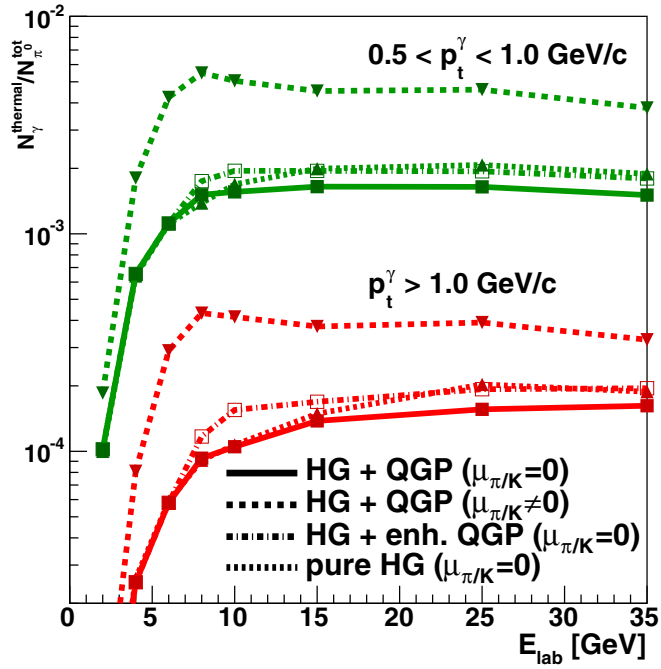

FIG. 13. Energy dependence for the ratio of thermal photon yield $N_\gamma^{\rm thermal}$ at midrapidity ($|y| < 0.5$) to the overall number N_{π^0} of neutral pions. The results are shown for two different regions of the photon transverse momenta: $0.5 < p_{\rm t} < 1.0$ GeV/c (green) and $p_{\rm t} > 1.0$ GeV/c (red). The baseline calculation assumes hadronic emission up to 170 MeV with vanishing μ_π and μ_K and partonic emission for higher temperatures (full line). In addition, the results are shown with a five-times-enhanced emission around the critical temperature (dashed-dotted line), for a pure-hadron-gas scenario with emission at all temperatures from hadronic sources (short dashed line), and including meson chemical potentials (dashed line).

1 GeV/c in case of the baseline scenario with QGP emission for $T > 170$ MeV and $\mu_\pi = 0$. However, for higher collision energies above 10A GeV we still observe a further increasing ratio for the higher-momentum range, whereas at low p_t the ratio remains relatively constant and even decreases for the highest collision energy. One can understand the decreasing ratio for lower p_t reviewing again the energy dependence of T and μ_B, as shown in Fig. 1. The rise of temperature becomes less intensive for higher collision energies, while the baryochemical potential decreases for higher collision energies, causing a less pronounced increase of the thermal yield (compare also Fig. 12). Besides, the effects due to finite μ_B are more pronounced at low momenta, explaining the different trends for the two p_t regions. Including finite meson chemical potentials, we observe a strong increase of the ratio by factors of two to five at all collision energies. The strongest effect in the present calculation is seen around 8A GeV, so that a slight peak structure builds up. However, as mentioned already several times, this scenario can only be seen as an upper limit for the nonequilibrium effects; most probably the increase will be smaller.

When comparing the two scenarios including enhanced QGP emission around T_c on the one side and a pure hadronic scenario on the other side, it is interesting that both cases lead to a similar result; namely, an increase of the N_γ/N_{π^0} ratio at higher collision energies. The effects show up more dominantly at high momenta, because this region is more sensitive with regard to emission from high temperatures. Note, however, that there are also significant differences between the two cases. The scenario with enhanced QGP emission around T_c shows the most prominent increase at $E_{lab} = 8A$–$10A$ GeV whereas this enhancement becomes smaller again for higher energies. This can be explained by the fact that the relative fraction of emission from temperatures around 170–175 MeV is largest at those collision energies where the transition to a partonic phase is just reached. At higher E_{lab}, the corresponding higher temperatures may outshine any effects from the transition region. On the contrary, the enhancement over the baseline scenario increases with energy for the case of a pure hadron gas. However, for the highest collision energies the difference seems to remain stable or even to drop again.

We remind the reader again that, for the experimental measurement, the ratio of thermal photons from Fig. 13 is of importance, because almost all of the π^0 mesons decay into a photon. Therefore the vast majority will be decay photons, not stemming from direct-emission (thermal- or prompt-emission) processes. Their spectra have to be subtracted in experiment to draw conclusions about the direct photons from thermal sources. This might be relatively difficult for the lowest energies available at FAIR, because here the ratio is suppressed by up to an order of magnitude compared with the higher collision energies.

V. DISCRIMINATING DIFFERENT SCENARIOS

It has so far become clear that one can extract only limited information regarding the properties of the hot and dense fireball from individual photon and dilepton spectra, because there are usually several different effects that might interfere and finally lead to the same invariant-mass or transverse-momentum yields. However, the picture could be quite different if—in addition—the results in distinct mass or momentum regions, respectively, are systematically compared for several collision energies. In this case one might be able to discriminate the hadronic and partonic effects from each other. The FAIR-energy regime will be ideally suited for such a study, because the transition from pure hadronic fireballs to the creation of a deconfined phase will take place somewhere around $E_{lab} = 6A$–$8A$ GeV, as our results suggest. Nevertheless, there is no single observable that seems to allow for unambiguous conclusions on the details of the reaction evolution. On the contrary, it will still be necessary to carefully compare theoretical calculations and experimental results.

Based on the findings of the present work, one may consider the following scheme which might help to determine the strength of the different effects on the thermal rates and discriminate between the contributions:

(1) The influence of baryonic matter leads to an enhancement which is most dominant for low transverse momenta and low masses. In general, it steepens the p_t slope of the overall yield. A large advantage is that, today, the spectral function of the ρ meson is quite well known from previous experimental and theoretical studies. Detailed and precise photon (dilepton) measurements for low momenta (low masses) in the FAIR- and RHIC-BES-energy regime might give further constraints on the spectral function in the region of extremely high baryon densities and can, vice versa, help to see whether the models correctly describe the fireball evolution in terms of μ_B.

(2) In contrast to the baryonic effects on the emission rates, nonequilibrium effects caused by finite pion (and kaon) chemical potentials will show up as enhancement in the dilepton and photon spectra at all masses and momenta and will be visible at all collision energies. The effect should be slightly more dominant in the high-invariant-mass or high-p_t region, because here the multimeson contributions become more pronounced. Ideally, one can discriminate between the μ_B- and μ_π-driven effects by comparing the modification of the slope and the overall enhancement in relation to baseline calculations.

(3) If the baryon and nonequilibrium effects are under control, one might be able to find signals from the partonic phase in the dilepton and photon spectra for high p_t and $M_{e^+e^-}$. In general, the dilepton and photon rates do not differ much from each other around T_c, but effects such as a critical slowdown of the evolution may lead to an increased yield from the quark-gluon plasma. On the other hand, the "duality mismatch" might lead to a relative decrease of the yield, because hadronic rates are sensitive to finite baryon and meson chemical potentials while the QGP rates show hardly any modification. However, any effects connected to a phase transition can only show up if the obtained temperatures are large enough. Consequently, we

would observe subsequent modifications of the spectra only for energies larger than $E_{\rm lab} = 6A$–$8A$ GeV, in contrast to nonequilibrium and baryonic effects which also appear at lower temperatures. Significant differences from calculations which *only* show up for the higher energies might then indicate the creation of a deconfined phase.

(4) Furthermore, these effects indicating a phase transition should be dominant in the regions which are most sensitive to QGP formation: For $M_{e^+e^-} > 1$ GeV in the dilepton spectra, and for high $p_{\rm t}$ in the photon, respectively, low-mass dilepton spectra (provided it is possible to get control over the hadronic decay background). Another advantage in these regions is that they are relatively insensitive to the finite baryon chemical potential.

The different issues are not easy to disentangle and several interdependencies exist. Another aspect, which is not explicitly considered in our work but might further complicate the situation, is the influence of different EoSs on the thermal yields. In the present work we use a hadron-gas EoS to provide consistency with the underlying microscopic model. However, previous investigations in a transport + hydrodynamics hybrid model showed that an MIT bag model EoS or a chiral EoS lead to different evolutions in the hydrodynamic phase compared with the HG-EoS, resulting in higher temperatures and, consequently, an increase in the emission rates.

VI. CONCLUSIONS AND OUTLOOK

We presented photon and dilepton spectra for the collision energy range $E_{\rm lab} = 2A$–$35A$ GeV, which will be covered by the future FAIR facility (and, in part, by phase II of the BES at RHIC). The calculations were performed by using a coarse-graining approach with transport simulations from the UrQMD model as input. In this approach local particle and energy densities are extracted from an ensemble average of the microscopic calculations, and an equation of state is used to calculate the corresponding values for temperature and chemical potential. The local thermodynamic properties are then used to determine the thermal emission rates.

The resulting spectra show a strong influence of finite baryochemical potentials and an enhancement due to nonequilibrium effects caused by finite meson chemical potentials. Regarding the search for signals of the deconfinement phase transition, there is no clear signal from which the creation of a partonic phase can be unambiguously inferred. Similarly, the results suggest that it is also hard to identify the type of the transition, whether it is a crossover or a first-order phase transition, because effects due to a critical slowing down might be small compared with other influences on the spectra. The main difficulty is the dual connection between hadronic and partonic emission rates in the transition region around the critical temperature $T_{\rm c}$, resulting in very similar slopes in the invariant-mass and transverse-momentum spectra.

For a clarification of the open issues, experimental input is needed. Our results suggest that one needs very precise and detailed measurements, because different evolution scenarios for the nuclear collisions are modifying the dilepton and photon spectra in a quite subtle manner. Systematic studies of several collision energies in the future FAIR energy range from $E_{\rm lab} = 2A$ to $35A$ GeV are required to get more insight into the structure of the phase diagram of QCD matter and especially to find clues for the creation of a deconfined phase. Besides the experimental efforts, it will be similarly important to intensify the theoretical studies.

ACKNOWLEDGMENTS

The authors especially thank Ralf Rapp for providing the parametrizations of the spectral functions and many fruitful discussions. This work was supported by the Hessian Initiative for Excellence (LOEWE) through the Helmholtz International Center for FAIR (HIC for FAIR), the Bundesministerium für Bildung und Forschung, Germany (BMBF) and the Helmholtz-Gemeinschaft through the Research School for Quark-Matter Studies (H-QM).

[1] H. Stöcker and W. Greiner, Phys. Rep. **137**, 277 (1986).
[2] P. Danielewicz, R. Lacey, and W. G. Lynch, Science **298**, 1592 (2002).
[3] J. D. Bjorken, Phys. Rev. D **27**, 140 (1983).
[4] R. Stock, *Physics and Methods - Theory and Experiments*, Landolt–Börnstein - Group I Elementary Particles, Nuclei and Atoms, Vol 21A, edited by H. Schopper (Springer, Berlin, 2010).
[5] E. L. Feinberg, II Nuovo Cimento A **34**, 391 (1976).
[6] E. V. Shuryak, Phys. Lett. B **78**, 150 (1978).
[7] D. Adamova *et al.* (CERES/NA45 Collaboration), Phys. Rev. Lett. **91**, 042301 (2003).
[8] M. M. Aggarwal *et al.* (WA98 Collaboration), Phys. Rev. Lett. **85**, 3595 (2000).
[9] R. Arnaldi, R. Averbeck, K. Banicz, J. Castor, B. Chaurand, C. Cicalo, A. Colla, P. Cortese, S. Damjanovic, A. David, A. DeFalco, A. Devaux, A. Drees, L. Ducroux, H. Enyo, J. Fargeix, A. Ferretti, M. Floris, A. Forster, P. Force, N. Guettet, A. Guichard, H. Gulkanian, J. M. Heuser, M. Keil, L. Kluberg, C. Lourenco, J. Lozano, F. Manso, A. Masoni, P. Martins, A. Neves, H. Ohnishi, C. Oppedisano, P. Parracho, P. Pillot, G. Puddu, E. Radermacher, P. Ramalhete, P. Rosinsky, E. Scomparin, J. Seixas, S. Serci, R. Shahoyan, P. Sonderegger, H. J. Specht, R. Tieulent, G. Usai, R. Veenhof, and H. K. Wohri (NA60 Collaboration), Phys. Rev. Lett. **96**, 162302 (2006).
[10] L. Adamczyk *et al.* (STAR Collaboration), Phys. Rev. Lett. **113**, 022301 (2014); L. Adamczyk *et al.*, **113**, 049903 (2014).
[11] S. S. Adler *et al.* (PHENIX Collaboration), Phys. Rev. Lett. **94**, 232301 (2005).
[12] A. Adare *et al.* (PHENIX Collaboration), Phys. Rev. Lett. **104**, 132301 (2010).
[13] A. Adare *et al.* (PHENIX), Phys. Rev. C **93**, 014904 (2016).
[14] M. K. Koehler (ALICE Collaboration), Nucl. Phys. A **931**, 665 (2014).
[15] R. J. Porter, S. Beedoe, R. Bossingham, M. Bougteb, W. B. Christie, J. Carroll, W. G. Gong, T. Hallman, L. Heilbronn, H. Z. Huang, G. Igo, P. Kirk, G. Krebs, A. Letessier-Selvon, L. Madansky, F. Manso, H. S. Matis, J. Miller, C. Naudet, M. Prunet, G. Roche, L. S. Schroeder, P. Seidl, Z. F. Wang,

R. C. Welsh, W. K. Wilson, and A. Yegneswaran (The DLS Collaboration), Phys. Rev. Lett. **79**, 1229 (1997).
[16] G. Agakichiev *et al.* (HADES Collaboration), Phys. Rev. Lett. **98**, 052302 (2007).
[17] G. Agakishiev *et al.* (HADES Collaboration), Phys. Lett. B **663**, 43 (2008).
[18] G. Agakishiev *et al.* (HADES Collaboration), Phys. Rev. C **84**, 014902 (2011).
[19] B. Bäuchle and M. Bleicher, Phys. Rev. C **82**, 064901 (2010).
[20] H. van Hees, M. He, and R. Rapp, Nucl. Phys. A **933**, 256 (2015).
[21] O. Linnyk, V. Konchakovski, T. Steinert, W. Cassing, and E. L. Bratkovskaya, Phys. Rev. C **92**, 054914 (2015).
[22] S. Turbide, R. Rapp, and C. Gale, Phys. Rev. C **69**, 014903 (2004).
[23] W. Liu and R. Rapp, Nucl. Phys. A **796**, 101 (2007).
[24] N. P. M. Holt, P. M. Hohler, and R. Rapp, Nucl. Phys. A **945**, 1 (2015).
[25] R. Rapp and J. Wambach, Adv. Nucl. Phys. **25**, 1 (2000).
[26] R. Rapp, Adv. High Energy Phys. **2013**, 148253 (2013).
[27] S. Endres, H. van Hees, J. Weil, and M. Bleicher, Phys. Rev. C **91**, 054911 (2015).
[28] S. Endres, H. van Hees, J. Weil, and M. Bleicher, Phys. Rev. C **92**, 014911 (2015).
[29] B. Friman, C. Höhne, J. Knoll, S. Leupold, J. Randrup *et al.*, Lect. Notes Phys. **814**, 1 (2011).
[30] P. Senger, JPS Conf. Proc. **8**, 022001 (2015).
[31] G. Odyniec, EPJ Web Conf. **95**, 03027 (2015).
[32] A. N. Sissakian and A. S. Sorin (NICA Collaboration), J. Phys. G **36**, 064069 (2009).
[33] C. S. Fischer, J. Luecker, and J. A. Mueller, Phys. Lett. B **702**, 438 (2011).
[34] W. Cassing and E. L. Bratkovskaya, Phys. Rep. **308**, 65 (1999).
[35] K. Schmidt, E. Santini, S. Vogel, C. Sturm, M. Bleicher, and H. Stöcker, Phys. Rev. C **79**, 064908 (2009).
[36] J. Weil, H. van Hees, and U. Mosel, Eur. Phys. J. A **48**, 111 (2012).
[37] L. P. Kadanoff and G. Baym, *Quantum Statistical Mechanics: Green's Function Methods in Equilibrium and Non-Equilibrium Problems* (W. A. Benjamin, New York, 1962).
[38] E. L. Bratkovskaya, W. Cassing, R. Rapp, and J. Wambach, Nucl. Phys. A **634**, 168 (1998).
[39] E. L. Bratkovskaya, W. Cassing, and O. Linnyk, Phys. Lett. B **670**, 428 (2009).
[40] E. L. Bratkovskaya, J. Aichelin, M. Thomere, S. Vogel, and M. Bleicher, Phys. Rev. C **87**, 064907 (2013).
[41] B. Schenke and C. Greiner, Phys. Rev. C **73**, 034909 (2006).
[42] B. Schenke and C. Greiner, Phys. Rev. Lett. **98**, 022301 (2007).
[43] J. Weil, U. Mosel, and V. Metag, Phys. Lett. B **723**, 120 (2013).
[44] J. Berges, K. Boguslavski, S. Schlichting, and R. Venugopalan, Phys. Rev. D **92**, 096006 (2015).
[45] H. van Hees and R. Rapp, Phys. Rev. Lett. **97**, 102301 (2006).
[46] G. Vujanovic, C. Young, B. Schenke, R. Rapp, S. Jeon, and C. Gale, Phys. Rev. C **89**, 034904 (2014).
[47] P. Huovinen, M. Belkacem, P. J. Ellis, and J. I. Kapusta, Phys. Rev. C **66**, 014903 (2002).
[48] J. Steinheimer, M. Lorenz, F. Becattini, R. Stock, and M. Bleicher, arXiv:1603.02051.
[49] S. A. Bass, M. Belkacem, M. Bleicher, M. Brandstetter, L. Bravina *et al.*, Prog. Part. Nucl. Phys. **41**, 255 (1998).
[50] M. Bleicher, E. Zabrodin, C. Spieles, S. A. Bass, C. Ernst *et al.*, J. Phys. G **25**, 1859 (1999).
[51] H. Petersen, M. Bleicher, S. A. Bass, and H. Stöcker, arXiv:0805.0567.
[52] A. R. Bodmer and C. N. Panos, Phys. Rev. C **15**, 1342 (1977).
[53] J. J. Molitoris, J. B. Hoffer, H. Kruse, and H. Stöcker, Phys. Rev. Lett. **53**, 899 (1984).
[54] J. Aichelin, Phys. Rep. **202**, 233 (1991).
[55] C. Eckart, Phys. Rev. **58**, 919 (1940).
[56] L. Bravina, E. Zabrodin, M. I. Gorenstein, S. Bass, M. Belkacem *et al.*, Nucl. Phys. A **661**, 600 (1999).
[57] W. Florkowski and R. Ryblewski, Phys. Rev. C **83**, 034907 (2011).
[58] W. Florkowski, M. Martinez, R. Ryblewski, and M. Strickland, Nucl. Phys. A **904–905**, 803c (2013).
[59] D. Bandyopadhyay, M. Gorenstein, H. Stöcker, W. Greiner, and H. Sorge, Z. Phys. C: Part. Fields **58**, 461 (1993).
[60] P. Koch, Phys. Lett. B **288**, 187 (1992).
[61] J. Sollfrank, P. Koch, and U. W. Heinz, Z. Phys. C: Part. Fields **52**, 593 (1991).
[62] D. Zschiesche, S. Schramm, J. Schaffner-Bielich, H. Stöcker, and W. Greiner, Phys. Lett. B **547**, 7 (2002).
[63] M. He, R. J. Fries, and R. Rapp, Phys. Rev. C **85**, 044911 (2012).
[64] S. Leupold, V. Metag, and U. Mosel, Int. J. Mod. Phys. E **19**, 147 (2010).
[65] J. J. Sakurai, *Currents and Mesons* (University of Chicago Press, Chicago, 1969).
[66] F. Klingl, N. Kaiser, and W. Weise, Nucl. Phys. A **624**, 527 (1997).
[67] M. Post, S. Leupold, and U. Mosel, Nucl. Phys. A **689**, 753 (2001).
[68] D. Cabrera, E. Oset, and M. J. Vicente Vacas, Nucl. Phys. A **705**, 90 (2002).
[69] F. Riek and J. Knoll, Nucl. Phys. A **740**, 287 (2004).
[70] J. Ruppert and T. Renk, Phys. Rev. C **71**, 064903 (2005).
[71] R. Rapp, G. Chanfray, and J. Wambach, Nucl. Phys. A **617**, 472 (1997).
[72] R. Rapp and C. Gale, Phys. Rev. C **60**, 024903 (1999).
[73] R. Rapp and J. Wambach, Eur. Phys. J. A **6**, 415 (1999).
[74] H. van Hees and R. Rapp, Nucl. Phys. A **806**, 339 (2008).
[75] H. van Hees, C. Gale, and R. Rapp, Phys. Rev. C **84**, 054906 (2011).
[76] R. Rapp, J. Wambach, and H. van Hees, in *Relativistic Heavy Ion Physics*, Landolt-Börnstein - Group I Elementary Particles, Nuclei and Atoms, Vol. 23, edited by R. Stock (Springer, Berlin, 2010), pp. 134–175.
[77] R. Rapp, Phys. Rev. C **63**, 054907 (2001).
[78] M. Heffernan, P. Hohler, and R. Rapp, Phys. Rev. C **91**, 027902 (2015).
[79] R. Rapp (private communication).
[80] J. I. Kapusta, P. Lichard, and D. Seibert, Phys. Rev. D **44**, 2774 (1991); **47**, 4171 (1993).
[81] P. Aurenche, F. Gelis, H. Zaraket, and R. Kobes, Phys. Rev. D **58**, 085003 (1998).
[82] P. Aurenche, F. Gelis, and H. Zaraket, Phys. Rev. D **61**, 116001 (2000).
[83] P. B. Arnold, G. D. Moore, and L. G. Yaffe, J. High Energy Phys. 12 (2001) 009.
[84] J. Cleymans, J. Fingberg, and K. Redlich, Phys. Rev. D **35**, 2153 (1987).
[85] E. Braaten, R. D. Pisarski, and T.-C. Yuan, Phys. Rev. Lett. **64**, 2242 (1990).
[86] H.-T. Ding, A. Francis, O. Kaczmarek, F. Karsch, E. Laermann, and W. Soeldner, Phys. Rev. D **83**, 034504 (2011).